Computers & Fluids 38 (2009) 1731–1748

Contents lists available at ScienceDirect

Computers & Fluids

journal homepage: www.elsevier.com/locate/compfluid

ADER schemes on unstructured meshes for nonconservative hyperbolic systems: Applications to geophysical flows

Michael Dumbser [a,*], Manuel Castro [b], Carlos Parés [b], Eleuterio F. Toro [a]

[a] Laboratory of Applied Mathematics, University of Trento, Via Mesiano 77, I-38100 Trento, Italy
[b] Department of Mathematical Analysis, University of Málaga, Campus Teatinos s/n, E-29080 Málaga, Spain

ARTICLE INFO

Article history:
Received 6 November 2008
Received in revised form 4 February 2009
Accepted 21 March 2009
Available online 2 April 2009

ABSTRACT

We develop a new family of well-balanced path-conservative quadrature-free one-step ADER finite volume and discontinuous Galerkin finite element schemes on unstructured meshes for the solution of hyperbolic partial differential equations with non-conservative products and stiff source terms. The fully discrete formulation is derived using the recently developed framework of explicit one-step P_NP_M schemes of arbitrary high order of accuracy in space and time for conservative hyperbolic systems [Dumbser M, Balsara D, Toro EF, Munz CD. A unified framework for the construction of one-step finite-volume and discontinuous Galerkin schemes. J Comput Phys 2008;227:8209–53]. The two key ingredients of our high order approach are: first, the high order accurate P_NP_M reconstruction operator on unstructured meshes, using the WENO strategy presented in [Dumbser M, Käser M, Titarev VA Toro EF. Quadrature-free non-oscillatory finite volume schemes on unstructured meshes for nonlinear hyperbolic systems. J Comput Phys 2007;226:204–43] to ensure monotonicity at discontinuities, and second, a local space–time Galerkin scheme to predict the evolution of the reconstructed polynomial data inside each element during one time step to obtain a high order accurate one-step time discretization. This approach is also able to deal with stiff source terms as shown in [Dumbser M, Enaux C, Toro EF. Finite volume schemes of very high order of accuracy for stiff hyperbolic balance laws. J Comput Phys 2008;227:3971–4001]. These two key ingredients are combined with the recently developed path-conservative methods of Parés [Parés C. Numerical methods for nonconservative hyperbolic systems: a theoretical framework. SIAM J Numer Anal 2006;44:300–21] and Castro et al. [Castro MJ, Gallardo JM, Parés C. High-order finite volume schemes based on reconstruction of states for solving hyperbolic systems with nonconservative products. Applications to shallow-water systems. Math Comput 2006;75:1103–34] to treat the non-conservative products properly. We show applications of our method to the two-layer shallow water equations as well as applications to the recently published depth-averaged two-fluid flow model of Pitman and Le [Pitman EB, Le L. A two-fluid model for avalanche and debris flows. Philos Trans Roy Soc A 2005;363:1573–601].

© 2009 Elsevier Ltd. All rights reserved.

1. Introduction

Most PDE systems in physics and engineering that are directly derived from first principles can be cast into conservation law form

$$\frac{\partial}{\partial t}W + \nabla \cdot \underline{\underline{F}}(W) = S(W), \tag{1}$$

where W is the vector of conserved variables, $\underline{\underline{F}}(W) = (f(W), g(W), h(W))$ is the flux tensor and $S(W)$ denotes an algebraic source term that can model other physical effects such as reaction or friction. Up to now, the principle of conservation is the most powerful tool available to give insight into physical processes observed in nature. The connection between conservation laws and the symmetries of space and time was first discovered by Emmy Noether in [25]. Building a mathematical model upon conservation properties usually gives the most complete description of a physical system. Unfortunately, not all mathematical models in physics and engineering can be written in fully conservative form, but there remain some non-conservative differential terms that can not be cast into the form of Eq. (1). This is usually caused by some modeling assumptions or simplifications that have been introduced in the underlying conservation laws. In this case, the governing PDE is more conveniently written in the following quasi-linear form:

$$\frac{\partial}{\partial t}W + \underline{\underline{A}}(W) \cdot \nabla W = S(W) \tag{2}$$

* Corresponding author.
E-mail addresses: michael.dumbser@ing.unitn.it, michael.dumbser@unitn.it (M. Dumbser), castro@anamat.cie.uma.es (M. Castro), pares@anamat.cie.uma.es (C. Parés), toro@ing.unitn.it (E.F. Toro).

0045-7930/$ - see front matter © 2009 Elsevier Ltd. All rights reserved.
doi:10.1016/j.compfluid.2009.03.008

with the system matrix $\underline{\underline{A}}(W) = (A(W), B(W), C(W))$. Here, we use block-matrix syntax to obtain a compact and simple notation of the matrices $A(W)$, $B(W)$ and $C(W)$ in the x, y and z directions, respectively. In the case of a *balance* law according to Eq. (1) the system matrices are the Jacobian matrices of the flux functions, i.e. $A = \partial f/\partial W$, $B = \partial g/\partial W$ and $C = \partial h/\partial W$, and in the non-conservative case, $A(W)$, $B(W)$ and $C(W)$ are general nonlinear functions of the state vector W. This means that the formulation (2) is suitable to describe at the same time conservation laws and non-conservative systems. In this article, we will cast all governing PDE in the general form given by Eq. (2) and also the numerical methods will be applied to PDE systems written in this way. In (2), $S(W)$ denotes again the source term modeling the reaction or friction effects. Following a strategy introduced in [21] geometrical source terms are included in the term $\underline{\underline{A}}(W) \cdot \nabla W$, which makes the design of well-balanced numerical schemes easier.

The main problem of equations of the form (2) is the lack of a classical definition of weak solutions of the PDE in the presence of discontinuities. The recently developed theory of Dal Maso et al. [23], called DLM theory in the following, led to significant progress, both, on the theoretical side as well as concerning numerical algorithm development for systems like (2). The DLM theory defines the weak solutions of (2) introducing a path $\mathbf{\Psi} = \mathbf{\Psi}(W_L, W_R, s)$ connecting the two states W_L and W_R in phase-space across a discontinuity. As a consequence, the weak solution of the non-conservative system then depends on the choice of the path $\mathbf{\Psi}$. With the unit tensor $\underline{\underline{I}}$ the resulting generalized Rankine–Hugoniot conditions for an isolated discontinuity travelling in direction $\vec{n}$ with speed σ reads

$$0 = \int_{s=0}^{1} (\underline{\underline{A}}(\mathbf{\Psi}(W_L, W_R, s)) \cdot \vec{n} - \sigma \underline{\underline{I}}) \frac{\partial \mathbf{\Psi}}{\partial s} ds. \tag{3}$$

From (3) it is obvious that for conservative systems, the DLM theory reproduces the classical Rankine–Hugoniot conditions across discontinuities, independent of the choice of $\mathbf{\Psi}$.

For general multi-dimensional systems, the path connecting two states W_L, W_R may also depend on $\vec{n}$, but if the system is rotationally invariant, as it will be supposed here, this dependency can be dropped, see [6]. The DLM theory is also useful for the design of numerical methods for nonconservative systems: Parés has introduced in [26] a theoretical framework based on the concept of path-conservative methods, which is a generalization of the usual concept of conservative methods for systems of conservation laws. The generalized Roe schemes introduced by Toumi in [36] constitute a particular case of path-conservative methods. This framework has been used in several papers to design high order numerical methods in one and two dimensions on structured meshes, both in the finite volume framework [8,18,24,7,10,6] and the discontinuous Galerkin finite element framework [32]. The design of second order finite volume methods in two dimensions on unstructured meshes has been considered by Castro et al. in [5]. However, to our knowledge, up to now there exists no path-conservative higher than second order accurate WENO and DG scheme yet on *unstructured* triangular meshes that is also able to deal with stiff source terms. The development of such schemes is the declared scope of the present article.

We underline that very recently Castro et al. [9] have shown that a path-conservative numerical method does not always guarantee the convergence of the numerical method to the weak solution given by the chosen path $\mathbf{\Psi}$. This deficiency seems to appear only in the computation of genuinely non-linear waves, whereas in many systems of relevance in physics and engineering, the discontinuities associated to the non-conservative products are linear degenerate. Moreover, even in the case of non-linear waves, this lack of convergence is only noticeable for very fine meshes, for discontinuities of great amplitude, or for large-time simulations, see [9]. A detailed study on the influence of the choice of paths $\mathbf{\Psi}$ for particular systems of interest in environmental engineering can also be found in [32].

The structure of the present article is as follows: in Section 2 we present our high order accurate numerical method on unstructured meshes. The general $P_N P_M$ reconstruction operator, introduced in [12], is briefly reviewed in Section 2.1. The local space–time predictors that allow us to construct high order accurate *one-step* methods in time are described in Section 2.2 and the fully discrete version of the final ADER schemes is presented in 2.3. The two systems of governing equations under consideration in the present article are described in Section 3, namely the two-layer shallow water system and the two-fluid debris flow and avalanche model of Pitman and Le [29] in the formulation of Pelanti et al. [28]. In order to show the high order of accuracy of our methods in space and time we invent two new *unsteady* and *genuinely two-dimensional* test cases with *analytical solution* in Section 4 for both, the two-layer shallow water system as well as for the two-fluid flow model of Pitman and Le. Finally, we present some applications in Section 5.

2. Numerical method

2.1. The $P_N P_M$ reconstruction operator on unstructured meshes

The main ingredient of the proposed numerical method to reach high order of accuracy in space is the $P_N P_M$ reconstruction operator on unstructured meshes first introduced in [12]. It is a direct extension of the reconstruction algorithm proposed in [14,15] for finite volume schemes. For the details, we refer to the above-mentioned publications and give only a short review in this section. The computational domain Ω is discretized by conforming elements T_i, indexed by a single mono-index i ranging from 1 to the total number of elements N_E. The elements are chosen to be triangles in 2D and tetrahedrons in 3D. The union of all elements is called the triangulation or tetrahedrization of the domain, respectively,

$$\mathscr{T}_\Omega = \bigcup_{i=1}^{N_E} T_i. \tag{4}$$

At the beginning of a time-step, the numerical solution of (2) for the state vector W, denoted by u_h, is represented by piecewise polynomials of degree N from the space V_h, spanned by the basis functions $\Phi_l = \Phi_l(\vec{x})$, i.e. at $t = t^n$ we have for each element

$$u_h(\vec{x}, t^n) = \sum_l \Phi_l(\vec{x}) \hat{u}_l^n. \tag{5}$$

From the polynomials u_h, we then reconstruct piecewise polynomials w_h of degree $M \geqslant N$ from the space W_h, spanned by the basis functions $\Psi_l = \Psi_l(\vec{x})$. As stated in [12], the Ψ_l form an orthogonal basis and are identical with the Φ_l up to polynomial degree N. For performing the reconstruction on element T_i, we now choose a reconstruction stencil

$$\mathscr{S}_i = \bigcup_{k=1}^{n_e} T_{j(k)} \tag{6}$$

that contains a total number of n_e elements. Here $1 \leqslant k \leqslant n_e$ is a local index, counting the elements in the stencil, and $j = j(k)$ is the mapping from the local index k to the global indexation of the elements in $\mathscr{T}_\Omega$. For ease of notation, we write in the following only j, meaning $j = j(k)$.

In the present paper the three operators

$$\langle f,g\rangle_{T_i} = \int_{t^n}^{t^{n+1}} \int_{T_i} (f(\vec{x},t)\cdot g(\vec{x},t))dV\,dt, \tag{7}$$

$$[f,g]^t_{T_i} = \int_{T_i} (f(\vec{x},t)\cdot g(\vec{x},t))dV, \tag{8}$$

$$\{f,g\}_{\partial T_i} = \int_{t^n}^{t^{n+1}} \int_{\partial T_i} (f(\vec{x},t)\cdot g(\vec{x},t))dS\,dt, \tag{9}$$

denote the scalar products of two functions f and g over the space–time element $T_i \times [t^n; t^{n+1}]$, the spatial element T_i, and the space–time boundary element $\partial T_i \times [t^n; t^{n+1}]$, respectively. The operators $\langle f,g\rangle$ and $[f,g]^t$, written without the index T_i, will denote scalar products on the space–time reference element $T_E \times [0;1]$ and on the spatial reference element T_E at time t, respectively. The spatial reference element T_E is defined as the unit simplex with vertices $(0,0),(1,0),(0,1)$ in two space dimensions and vertices $(0,0,0)$, $(1,0,0)$, $(0,1,0)$ and $(0,0,1)$ in three space dimensions, respectively.

The reconstruction is now obtained via L_2-projection of the (unknown) piecewise polynomials w_h from the space W_h into the space V_h on each stencil $\mathscr{S}_i$ as follows:

$$[\Phi_k, w_h]^{t^n}_{T_j} = [\Phi_k, u_h]^{t^n}_{T_j} \quad \forall T_j \in \mathscr{S}_i. \tag{10}$$

Note that during the reconstruction step, the polynomials w_h are continuously extended over the whole stencil $\mathscr{S}_i$. After reconstruction, the piecewise polynomials w_h are again restricted onto each element T_i. The number of elements in the stencils are chosen in such a way that the number of equations in (10) is *larger* that the number of degrees of freedom in the space W_h. Eq. (10) constitutes thus an overdetermined linear algebraic equation system for the coefficients of w_h and is solved using a constrained least squares technique, see [12,14]. The linear constraint is that Eq. (10) is at least exactly satisfied for $T_j = T_i$, i.e. inside the element T_i under consideration. The integral on the left-hand side in (10) is computed using classical multi-dimensional Gaussian quadrature of appropriate order, see [33]. The integral on the right-hand side can be computed analytically and involves the standard element mass-matrix. The resulting M-exact $P_N P_M$ least squares reconstruction can be interpreted as a generalization of the k-exact reconstruction proposed for pure finite volume schemes by Barth and Frederickson in their pioneering work [2]. For problems with shock waves, we resort to the classical WENO finite volume version ($P_0 P_M$ schemes) with characteristic reconstruction as described in [15].

2.2. The local space–time Galerkin predictor

The original ENO scheme of Harten et al. [19] as well as the ADER-FV and ADER-DG schemes developed by Titarev and Toro [34] and Dumbser and Munz [17] use the governing PDE itself in its strong differential form to obtain high order of accuracy in time. This is achieved via the so-called Cauchy–Kovalewski procedure that substitutes time derivatives with space derivatives via successive differentiation of the governing PDE with respect to space and time. This procedure becomes very cumbersome or even impossible for general nonlinear hyperbolic PDE systems. In [13,12], an entirely numerical approach was presented that replaces the Cauchy–Kovalewski procedure by a *local weak formulation* of the governing PDE in space–time. While the approach presented in [13] relies on a local discontinuous Galerkin approach in space–time, which is also able to handle stiff source terms, the method proposed in [12] uses a local continuous Galerkin method in space–time as predictor. In the present article we use both approaches, depending on the stiffness of the source terms. For non-stiff problems, we shall use the local continuous Galerkin method in space–time, for stiff problems we use the local discontinuous Galerkin method in space–time. The selection between one or the other method is done in an automatic way. First, the local continuous space–time method is tried since it is computationally cheaper. If the iteration scheme (which is a contraction in the non-stiff case) does diverge, then automatically the local discontinuous Galerkin space–time method is used, which works also in the stiff case. The selection is done element-by-element in each time step. We underline that both local space–time Galerkin methods are only used as *local predictors* for the construction of a solution of the PDE *in the small*, as it was called by Harten et al. in [19]. The local space–time predictors are then inserted into a *global corrector*, which is fully explicit and provides the coupling between neighbor cells. As a consequence, the resulting nonlinear algebraic systems of the local space–time Galerkin methods are element local and not globally coupled, as in the global and fully implicit space–time Galerkin approach introduced by van der Vegt and van der Ven [37,38].

2.2.1. Local continuous space–time Galerkin method

We start from the strong formulation of PDE (2) in two space dimensions and first transform the PDE into the reference coordinate system $(\vec{\xi},\tau)$ with $\vec{\xi} = (\xi,\eta)$ of the space–time reference element $T_E \times [0;1]$:

$$\frac{\partial}{\partial\tau}W + A^*\frac{\partial}{\partial\xi}W + B^*\frac{\partial}{\partial\eta}W = S^*. \tag{11}$$

The modified system matrices and the modified source term are given by

$$\begin{aligned} &A^* := \Delta t(A(W)\xi_x + B(W)\xi_y), \quad B^* := \Delta t(A(W)\eta_x + B(W)\eta_y), \\ &S^* := \Delta t S(W), \end{aligned} \tag{12}$$

as one can show by simple algebraic manipulations. We now multiply Eq. (11) by a space–time test function $\theta_k = \theta_k(\xi,\eta,\tau)$ from the space of piecewise space–time polynomials of degree M and integrate over the space–time reference control volume $T_E \times [0;1]$ to obtain the following weak formulation:

$$\left\langle \theta_k, \frac{\partial}{\partial\tau}\mathscr{W}_h \right\rangle + \left\langle \theta_k, A^*\frac{\partial}{\partial\xi}\mathscr{W}_h \right\rangle + \left\langle \theta_k, B^*\frac{\partial}{\partial\eta}\mathscr{W}_h \right\rangle = \langle \theta_k, S^*\rangle. \tag{13}$$

For the solution of Eq. (13) we make the ansatz

$$\mathscr{W}_h = \mathscr{W}_h(\xi,\eta,\tau) = \sum_l \theta_l(\xi,\eta,\tau)\widehat{\mathscr{W}}_l := \theta_l\widehat{\mathscr{W}}_l, \tag{14}$$

using the same space–time basis functions θ_l as used for the test functions. To facilitate notation, from now on we use the Einstein summation convention throughout the paper, which implies summation over indices appearing twice. We use the nodal space–time basis and test functions θ_k proposed in [12].

Whereas for conservative systems one only has to interpolate the physical fluxes f and g, in the non-conservative case we now must interpolate the products of the modified system matrices A^* and B^* with the spatial derivatives of $\mathscr{W}_h$. We use the ansatz

$$A^*\frac{\partial\mathscr{W}_h}{\partial\xi} := \theta_l A^*\widehat{\partial_\xi\mathscr{W}}_l, \quad B^*\frac{\partial\mathscr{W}_h}{\partial\eta} := \theta_l B^*\widehat{\partial_\eta\mathscr{W}}_l, \quad S^* := \theta_l\widehat{S}^*_l. \tag{15}$$

In our implementation we choose a nodal interpolation so that

$$\begin{aligned} &A^*\widehat{\partial_\xi\mathscr{W}}_l = A^*\left.\frac{\partial\mathscr{W}_h}{\partial\xi}\right|_{\vec{\xi}=\vec{\xi}_l}, \quad B^*\widehat{\partial_\eta\mathscr{W}}_l = B^*\left.\frac{\partial\mathscr{W}_h}{\partial\eta}\right|_{\vec{\xi}=\vec{\xi}_l}, \\ &\widehat{S}^*_l = S^*(\mathscr{W}_h)|_{\vec{\xi}=\vec{\xi}_l}, \end{aligned} \tag{16}$$

which is computationally more efficient than L_2-projection via Gaussian quadrature formulae.

To solve the weak form (13) we insert (15) and (16) into (13) and then use the following fixed-point iteration scheme:

$$\left\langle \theta_k, \frac{\partial}{\partial \tau}\theta_l \right\rangle \widehat{\mathscr{W}_l}^{i+1} = \langle \theta_k, \theta_l \rangle \left(\widehat{S_l^*}^i - A^* \widehat{\partial_\xi \mathscr{W}_l}^i - B^* \widehat{\partial_\eta \mathscr{W}_l}^i \right). \tag{17}$$

To include the initial condition in (17) we proceed as usual in the continuous Galerkin finite element framework, fixing the known degrees of freedom at relative time $\tau = 0$. Therefore, we split the coefficient vector $\widehat{\mathscr{W}_l}$ as $\widehat{\mathscr{W}_l} = (\widehat{\mathscr{W}_l^0}, \widehat{\mathscr{W}_l^1})^T$, where $\widehat{\mathscr{W}_l^0}$ are the known degrees of freedom at relative time $\tau = 0$ and $\widehat{\mathscr{W}_l^1}$ are the unknown degrees of freedom for $\tau > 0$. From (17) we therefore only need the equations for the unknowns $\widehat{\mathscr{W}_l^1}$. Further details of this algorithm are given in [12].

2.2.2. Local discontinuous space–time Galerkin method

To derive the non-conservative equivalent for the local discontinuous space–time Galerkin method proposed in [13] we directly start from the weak formulation given by Eq. (13) and apply integration by parts to the first term. This gives the following element-local weak formulation of (2),

$$[\theta_k, \mathscr{W}_h]^1 - [\theta_k, w_h]^0 - \left\langle \frac{\partial}{\partial \tau}\theta_k, \mathscr{W}_h \right\rangle + \left\langle \theta_k, A^* \frac{\partial}{\partial \xi}\mathscr{W}_h \right\rangle + \left\langle \theta_k, B^* \frac{\partial}{\partial \eta}\mathscr{W}_h \right\rangle = \langle \theta_k, S^* \rangle, \tag{18}$$

where the initial condition at relative time $\tau = 0$ is taken into account in a *weak sense* by the term $[\theta_k, w_h]^0$. Remember that w_h is the piecewise polynomial obtained by the high order $P_N P_M$ reconstruction operator summarized in 2.1. Note that the first two terms in (18) correspond to the choice of an upwind flux in the time direction, which is consistent with the causality principle that states that no effect can occur before its cause.

Eq. (18) leads to element-local nonlinear algebraic systems that can be solved using e.g. a globally convergent Newton method, such as the one described in [30].

2.3. The fully discrete ADER-NC scheme

We now have all the key ingredients to construct the final explicit one-step ADER $P_N P_M$ schemes. For this purpose we multiply the original governing Eq. (2) by a test function Φ_k from the space V_h and integrate the PDE over the space–time element $T_i \times [t^n; t^{n+1}]$, i.e. we apply the operator $\langle \Phi_k, \cdot \rangle_{T_i}$ to PDE (2) and obtain

$$\left\langle \Phi_k, \frac{\partial}{\partial t} W \right\rangle_{T_i} + \langle \Phi_k, \underline{\underline{A}}(W) \cdot \nabla W \rangle_{T_i} = \langle \Phi_k, S(W) \rangle_{T_i}. \tag{19}$$

For the first term in Eq. (19) we approximate W with u_h from the space V_h and perform integration by parts in time. Since Φ_k does not depend on time, the corresponding time derivative on Φ_k vanishes. For all the other terms in Eq. (19) W is approximated by the solution $\mathscr{W}_h$ of one of the two local space–time Galerkin predictor methods described in the previous Section 2.2. Since $\mathscr{W}_h$ will usually exhibit jumps at the element boundaries, we introduce a path-conservative method to account for these jumps and we obtain the following family of fully discrete one-step ADER $P_N P_M$ scheme for PDE (2):

$$\left[\Phi_k, u_h^{n+1}\right]_{T_i}^{t^{n+1}} - \left[\Phi_k, u_h^n\right]_{T_i}^{t^n} + \langle \Phi_k, \underline{\underline{A}}(\mathscr{W}_h) \cdot \nabla \mathscr{W}_h \rangle_{T_i \setminus \partial T_i} + \left\{ \Phi_k, \mathscr{D}^-\left(\mathscr{W}_h^-, \mathscr{W}_h^+, \vec{n}\right) \right\}_{\partial T_i} = \langle \Phi_k, S(\mathscr{W}_h) \rangle_{T_i}, \tag{20}$$

where $\mathscr{W}_h^-$ denotes the boundary extrapolated data from within element T_i and $\mathscr{W}_h^+$ denotes the boundary extrapolated data from the neighbor, respectively, and $\mathscr{D}^-$ is a function such that:

- For every $W, \vec{n}$

$$\mathscr{D}^-(W, W, \vec{n}) = 0. \tag{21}$$

- For every $\mathscr{W}_h^-, \mathscr{W}_h^+, \vec{n}$:

$$\mathscr{D}^-(\mathscr{W}_h^-, \mathscr{W}_h^+, \vec{n}) + \mathscr{D}^-(\mathscr{W}_h^+, \mathscr{W}_h^-, -\vec{n}) = \int_0^1 (\underline{\underline{A}}(\mathbf{\Psi}(\mathscr{W}_h^-, \mathscr{W}_h^+, s)) \cdot \vec{n}) \frac{\partial \mathbf{\Psi}}{\partial s} ds. \tag{22}$$

We recall that according to [12] the conservative equivalent of the $P_N P_M$ scheme (20) in order to solve conservation laws of the form (1) is given by

$$\left[\Phi_k, u_h^{n+1}\right]_{T_i}^{t^{n+1}} - \left[\Phi_k, u_h^n\right]_{T_i}^{t^n} - \langle \nabla \Phi_k \cdot \underline{\underline{F}}(\mathscr{W}_h) \rangle_{T_i \setminus \partial T_i} + \left\{ \Phi_k, \mathscr{G}_{i+\frac{1}{2}} \right\}_{\partial T_i} = \langle \Phi_k, S(\mathscr{W}_h) \rangle_{T_i} \tag{23}$$

with the numerical flux $\mathscr{G}_{i+\frac{1}{2}} = \mathscr{G}_{i+\frac{1}{2}}(\mathscr{W}_h^-, \mathscr{W}_h^+, \vec{n})$.

We now prove that the non-conservative $P_N P_M$ scheme (20) reduces to the conservative $P_N P_M$ scheme (23) in the case where the non-conservative system (2) is a conservation law (1), i.e. when the matrices A, B and C are the Jacobians of some flux functions f, g and h, respectively. In this case, obviously the following identity holds:

$$\langle \Phi_k, \underline{\underline{A}}(\mathscr{W}_h) \cdot \nabla \mathscr{W}_h \rangle_{T_i \setminus \partial T_i} = \langle \Phi_k, \nabla \cdot \underline{\underline{F}}(\mathscr{W}_h) \rangle_{T_i \setminus \partial T_i}. \tag{24}$$

Integration by parts of the term on the right-hand side yields

$$\langle \Phi_k, \nabla \cdot \underline{\underline{F}}(\mathscr{W}_h) \rangle_{T_i \setminus \partial T_i} = \{ \Phi_k, \underline{\underline{F}}(\mathscr{W}_h^-) \cdot \vec{n} \}_{\partial T_i} - \langle \nabla \Phi_k \cdot \underline{\underline{F}}(\mathscr{W}_h) \rangle_{T_i \setminus \partial T_i}. \tag{25}$$

Following [26], we define

$$\mathscr{G}_{i+\frac{1}{2}} = \mathscr{G}\left(\mathscr{W}_h^-, \mathscr{W}_h^+, \vec{n}\right) := \underline{\underline{F}}\left(\mathscr{W}_h^-\right) \cdot \vec{n} + \mathscr{D}^-\left(\mathscr{W}_h^-, \mathscr{W}_h^+, \vec{n}\right). \tag{26}$$

It can be easily checked that the function $\mathscr{G}$ satisfies

$$\mathscr{G}(W, W, \vec{n}) = \underline{\underline{F}}(W) \cdot \vec{n} \quad \forall W, \vec{n}, \tag{27}$$

$$\mathscr{G}\left(\mathscr{W}_h^+, \mathscr{W}_h^-, -\vec{n}\right) = -\mathscr{G}\left(\mathscr{W}_h^-, \mathscr{W}_h^+, \vec{n}\right), \tag{28}$$

and it defines thus a consistent numerical flux.

Inserting Eqs. (26), (24) and (25) into Eq. (20) yields directly the conservative $P_N P_M$ scheme (23), which completes the proof that the path-conservative $P_N P_M$ method (20) reduces to the conservative $P_N P_M$ scheme (23) in the case where the non-conservative system (2) reduces to a system of conservation laws (1).

In particular, Roe-type methods correspond to the choice:

$$D^-\left(\mathscr{W}_h^-, \mathscr{W}_h^+, \vec{n}\right) = \left(\underline{\underline{\widetilde{A}}}_{\mathbf{\Psi}}\left(\mathscr{W}_h^-, \mathscr{W}_h^+\right) \cdot \vec{n}\right)^- \left(\mathscr{W}_h^+ - \mathscr{W}_h^-\right), \tag{29}$$

where $\underline{\underline{\widetilde{A}}}_{\mathbf{\Psi}}\left(\mathscr{W}_h^-, \mathscr{W}_h^+\right)$ is a Roe-type matrix satisfying the generalized Rankine–Hugoniot conditions

$$\left(\underline{\underline{\widetilde{A}}}_{\mathbf{\Psi}}\left(\mathscr{W}_h^-, \mathscr{W}_h^+\right) \cdot \vec{n}\right)\left(\mathscr{W}_h^+ - \mathscr{W}_h^-\right) = \int_0^1 \left(\underline{\underline{A}}\left(\mathbf{\Psi}\left(\mathscr{W}_h^-, \mathscr{W}_h^+, s\right)\right) \cdot \vec{n}\right) \frac{\partial \mathbf{\Psi}}{\partial s} ds, \tag{30}$$

and where the usual definitions apply:

$$Z^- = R\Lambda^- R^{-1} = \frac{1}{2}(Z - |Z|), \quad |Z| = R|\Lambda|R^{-1}, \quad \Lambda^- = \frac{1}{2}(\Lambda - |\Lambda|), \tag{31}$$

with R being the matrix of right eigenvectors of a general matrix Z. Λ^- is, as usual, the negative part of the diagonal matrix Λ containing the eigenvalues of Z. All operators applied on Λ are applied componentwise on its diagonal elements. It can be easily verified that, for conservative problems, the numerical flux defined by (26) is in this case the usual Roe flux:

$$\mathscr{G}_{i+\frac{1}{2}} = \frac{1}{2}\left(\underline{\underline{F}}(\mathscr{W}_h^+) + \underline{\underline{F}}(\mathscr{W}_h^-)\right)\cdot\vec{n} - \frac{1}{2}\left|\underline{\underline{\widetilde{A}}}_{\mathbf{\Psi}}(\mathscr{W}_h^-, \mathscr{W}_h^+)\cdot\vec{n}\right|(\mathscr{W}_h^+ - \mathscr{W}_h^-). \tag{32}$$

As a cheaper alternative to the Roe-type method used in (20), which requires the computation of all eigenvalues and eigenvectors of the Roe matrix $(\underline{\underline{\widetilde{A}}}_{\mathbf{\Psi}}\cdot\vec{n})$, a non-conservative equivalent of the Rusanov flux may be used, see [9,10], which is given by

$$\mathscr{D}^-(\mathscr{W}_h^-, \mathscr{W}_h^+, \vec{n}) := \frac{1}{2}\left(\underline{\underline{\widetilde{A}}}_{\mathbf{\Psi}}(\mathscr{W}_h^-, \mathscr{W}_h^+)\cdot\vec{n} - |\lambda_{\max}|\underline{\underline{I}}\right)(\mathscr{W}_h^+ - \mathscr{W}_h^-), \tag{33}$$

where $\underline{\underline{I}}$ is the identity matrix, $|\lambda_{\max}|$ denotes the maximum absolute value of the eigenvalues of the matrices $\underline{\underline{A}}(\mathscr{W}_h^-)\cdot\vec{n}$ and $\underline{\underline{A}}(\mathscr{W}_h^+)\cdot\vec{n}$, respectively. For conservative problems, it is trivial to prove that the numerical flux defined by (26) reduces now to the Rusanov flux:

$$\mathscr{G}_{i+\frac{1}{2}} = \frac{1}{2}\left(\underline{\underline{F}}(\mathscr{W}_h^+) + \underline{\underline{F}}(\mathscr{W}_h^-)\right)\cdot\vec{n} - \frac{1}{2}|\lambda_{\max}|(\mathscr{W}_h^+ - \mathscr{W}_h^-). \tag{34}$$

For all simulations shown in this paper, however, we use the *Roe-type* scheme. All the Roe linearizations considered are based on the family of segments:

$$\mathbf{\Psi}(\mathscr{W}_h^-, \mathscr{W}_h^+, s) = \mathscr{W}_h^- + s(\mathscr{W}_h^+ - \mathscr{W}_h^-). \tag{35}$$

2.4. Well-balanced properties

In order to avoid the appearing of spurious oscillations when approaching equilibria or solutions close to equilibria, the numerical schemes are required to solve *exactly* a family of predetermined stationary solutions. For instance, in the context of shallow water systems, numerical methods are usually required to satisfy the C-property introduced in [3]: they have to solve exactly the stationary solutions corresponding to water at rest.

We only consider here stationary solutions $W(\vec{x})$ of (2) for which $S(W) = 0$, i.e. W is a solution of the homogeneous problem

$$\underline{\underline{A}}(W)\cdot\nabla W = 0. \tag{36}$$

Remember that geometrical source terms have already been taken into account in these homogeneous problems, since they have been included in the tensor $\underline{\underline{A}}$ and in the unknowns W. Let us suppose that the numerical schemes are required to solve exactly the solutions of (36) belonging to a certain family Γ. Two states W^- and W^+ are said to be *reachable* if there exist $W \in \Gamma$ and $\vec{x}, \vec{y}$ such that:

$$W^- = W(\vec{x}), \quad W^+ = W(\vec{y}). \tag{37}$$

It can be easily verified that the numerical scheme solves exactly the solution of the family Γ provided that:

- The reconstruction is well-balanced in the following sense: for any stationary solution W of Γ
  - for every T_j the approximation $u_h \in V_h$ of W is a stationary solution of the same family Γ and its reconstruction w_h is equal to u_h;
  - the extrapolations $\mathscr{W}_h^-, \mathscr{W}_h^+$ at every point of every boundary ∂T_i are reachable.
- The first order path-conservative numerical scheme is well-balanced in the following sense: if W^-, W^+ are reachable then

$$\mathscr{D}^-(W^-, W^+, \vec{n}) = 0 \quad \forall\vec{n}. \tag{38}$$

In effect, if these well-balanced properties are satisfied and the initial condition is a solution of the family Γ it can be easily verified that, for $N = 0$ and $M = 0$, all the terms in (20) vanish except for the two first terms of the left-hand side.

The well-balanced properties of Roe methods have been extensively studied in [27]. In general, they are strongly related to the choice of the family of paths. Rusanov methods are not well-balanced in general, but it is possible to modify them to have the same well-balanced properties as Roe-type schemes. For this, the identity matrix in (33) has to be modified (see [10]). Since this modification, however, has to be carried out specifically for each governing PDE, we will give more details in the next section, where we describe the particular PDE systems under consideration in this article.

2.5. Quadrature-free implementation

We would like to note that also in the non-conservative case it is possible to use a quadrature-free implementation, exactly as proposed in [15,12]. In this section we briefly recall the formulation and for further details we refer the reader to the above-mentioned articles. The main idea consists of computing a leading term of the boundary integrals $\{\Phi_k, \mathscr{D}^-\}_{\partial\mathscr{T}_i}$ in the space–time barycenter of the boundary face (this corresponds to a second order accurate Gaussian quadrature rule) and then use a *linearized* model of the higher order variations of the operator $\mathscr{D}^-$ that can then be integrated *analytically*. The quadrature-free one-step formulation of the Roe-type method (20) and (29) can thus be written as follows:

$$\begin{aligned}
&[\Phi_k, \Phi_l](\hat{u}_l^{n+1} - \hat{u}_l^n) + \Delta t\sum_{j=1}^{N_E}\frac{|\partial T_j|}{|T_i|}F_k^{0,j}\mathscr{D}^-(\overline{\mathscr{W}}_h^-, \overline{\mathscr{W}}_h^+, \vec{n}_j)\\
&\quad + \Delta t\sum_{j=1}^{N_E}\frac{|\partial T_j|}{|T_i|}\left(\underline{\underline{\widetilde{A}}}_{\mathbf{\Psi}}(\overline{\mathscr{W}}_h^-, \overline{\mathscr{W}}_h^+)\cdot\vec{n}\right)^-\left(F_{kl}^{+j}\widehat{\mathscr{W}}_l^+ - F_{kl}^{-j}\widehat{\mathscr{W}}_l^-\right)\\
&= \langle\Phi_k, \theta_l\rangle\left(\widehat{\mathscr{S}}_{lp}^* - A^*\widehat{\partial_\xi\mathscr{W}}_l - B^*\widehat{\partial_\eta\mathscr{W}}_l\right).
\end{aligned} \tag{39}$$

Here, $\overline{\mathscr{W}}_h^\pm$ denote the right and left values in the space–time barycenter of the boundary face ∂T_j and N_E the number of edges of the element. Due to the linearity of the high order corrector term in its arguments, which is achieved by *freezing* the matrix at its value in the space–time barycenter, flux computation and space–time integration can be exchanged. To perform this integration analytically, we introduce the following mesh-independent flux matrices, which have to be precomputed only once on one single reference element and then can be stored:

$$F_k^{0,j} = \int_0^1\int_{\partial T_E^j}\Phi_k^-\,dS\,d\tau, \tag{40}$$

$$\begin{aligned}
F_{kl}^{-j} &= \int_0^1\int_{\partial T_E^j}\Phi_k^-(\theta_l^- - \overline{\theta}_l^-)dS\,d\tau, \quad F_{kl}^{+j}\\
&= \int_0^1\int_{\partial T_E^j}\Phi_k^-(\theta_l^+ - \overline{\theta}_l^+)dS\,d\tau.
\end{aligned} \tag{41}$$

Here, ∂T_E^j denotes edge j of the reference element and the superscripts $-$ and $+$ denote the basis and test functions taken from within the element and of the neighbor element, respectively. Furthermore $\overline{\theta}_l^\pm$ denotes the space–time basis function evaluated in the space–time barycenter of edge j. For more details and some examples on unstructured triangular meshes we refer the reader to [12,15].

3. Governing equations

3.1. The two-layer shallow water equations

For the two-layer shallow water equations the vector of conserved quantities is $W = (h_1, h_1u_1, h_1v_1, h_2, h_2u_2, h_2v_2, b)^T$ and the system matrices $A(W)$ and $B(W)$ are given by

$$A(W)=\begin{bmatrix} 0 & 1 & 0 & 0 & 0 & 0 & 0 \\ -u_1^2+gh_1 & 2u_1 & 0 & gh_1 & 0 & 0 & gh_1 \\ -u_1v_1 & v_1 & u_1 & 0 & 0 & 0 & 0 \\ 0 & 0 & 0 & 0 & 1 & 0 & 0 \\ \rho gh_2 & 0 & 0 & -u_2^2+gh_2 & 2u_2 & 0 & gh_2 \\ 0 & 0 & 0 & -u_2v_2 & v_2 & u_2 & 0 \\ 0 & 0 & 0 & 0 & 0 & 0 & 0 \end{bmatrix}, \quad (42)$$

$$B(W)=\begin{bmatrix} 0 & 0 & 1 & 0 & 0 & 0 & 0 \\ -u_1v_1 & v_1 & u_1 & 0 & 0 & 0 & 0 \\ -v_1^2+gh_1 & 0 & 2v_1 & gh_1 & 0 & 0 & gh_1 \\ 0 & 0 & 0 & 0 & 0 & 1 & 0 \\ 0 & 0 & 0 & -u_2v_2 & v_2 & u_2 & 0 \\ \rho gh_2 & 0 & 0 & -v_2^2+gh_2 & 0 & 2v_2 & gh_2 \\ 0 & 0 & 0 & 0 & 0 & 0 & 0 \end{bmatrix}. \quad (43)$$

Here, g is the gravity constant and $\rho=\rho_1/\rho_2$ is the density ratio between the upper fluid (index 1) and the lower fluid (index 2). The bottom topography is given by b. In the following sections, we will also use the total free surface height $\eta=\eta_1=b+h_2+h_1$ and the free surface elevation of the interior layer $\eta_2=b+h_2$. The Roe averages for this system are given by

$$\tilde{h}_i=\frac{1}{2}(h_i^-+h_i^+), \quad \tilde{u}_i=\frac{\sqrt{h_i^-}u_i^-+\sqrt{h_i^+}u_i^+}{\sqrt{h_i^-}+\sqrt{h_i^+}},$$
$$\tilde{v}_i=\frac{\sqrt{h_i^-}v_i^-+\sqrt{h_i^+}v_i^+}{\sqrt{h_i^-}+\sqrt{h_i^+}}, \quad (44)$$

where the index i denotes either layer one or layer two.

The steady-state solution at rest for this system is described by the following relations:

$$h_1=const., \quad \eta=h_1+h_2+b=const., \quad u_1=u_2=v_1=v_2=0, \quad (45)$$

or in terms of the jumps

$$\Delta h_1=0, \quad \Delta h_2+\Delta b=0. \quad (46)$$

The numerical schemes described in this paper are required to solve exactly the family of stationary solutions given by (45). In this case, two states W^-, W^+ are said to be *reachable* if

$$h_1^-=h_1^+, \quad \eta^-=h_1^-+h_2^-+b^-=\eta^+=h_1^++h_2^++b^+,$$
$$u_1^-=u_1^+=u_2^-=u_2^+=v_1^-=v_1^+=v_2^-=v_2^+=0.$$

Following [27,6], it can be easily proved that if two states W^- and W^+ are reachable, then Roe-type method (29) based on the family of segments, is exactly well-balanced. It can be easily checked that when using the following "well-balanced" identity matrix $\underline{\underline{I}}^{WB}$ instead of $\underline{\underline{I}}$, the non-conservative Rusanov-type schemes will conserve exactly the steady-state solution (45), (46) at rest:

$$\underline{\underline{I}}^{WB}=\begin{pmatrix} 1 & 0 & 0 & 0 & 0 & 0 & 0 \\ 0 & 1 & 0 & 0 & 0 & 0 & 0 \\ 0 & 0 & 1 & 0 & 0 & 0 & 0 \\ 0 & 0 & 0 & 1 & 0 & 0 & 1 \\ 0 & 0 & 0 & 0 & 1 & 0 & 0 \\ 0 & 0 & 0 & 0 & 0 & 1 & 0 \\ 0 & 0 & 0 & 0 & 0 & 0 & 0 \end{pmatrix}. \quad (47)$$

Furthermore, the reconstruction is well-balanced in the sense defined in Section 2.4. In effect, when reconstruction is performed in the variables η, h_1 and b, then the resulting numerical schemes are *exactly* well-balanced for the stationary solution corresponding to water at rest (45).

3.2. The two-fluid flow model of Pitman and Le

For the two-fluid flow model of Pitman and Le [29] we consider the formulation given by Pelanti et al. in [28] since it yields a conservation law for the mixture, in contrast to the original equations of Pitman and Le. The vector of conserved quantities is in this case $W=(h_s, h_sv_x, h_sv_y, h_f, h_fu_x, h_fu_y, b)^T$ with $h_s=\phi h$ and $h_f=(1-\phi)h$. Here, h denotes the total depth, h_s and h_f the solid and the fluid depths, respectively, and ϕ is the solid volume fraction. The system matrices $A(W)$ and $B(W)$ for the two-dimensional Pitman and Le model [29] using the variant of Pelanti et al. [28] are given by

$$A(W)=\begin{bmatrix} 0 & 1 & 0 & 0 & 0 & 0 & 0 \\ \frac{1}{2}(T_1^{xx}+T_2^{xx})-v_x^2+\rho gh_s & 2v_x & 0 & \frac{1}{2}T_1^{xx}+g\rho h_s & 0 & 0 & T_1^{xx}+\rho gh_s \\ \frac{1}{2}(T_1^{xy}+T_2^{xy})-v_xv_y & v_y & v_x & \frac{1}{2}T_1^{xy} & 0 & 0 & T_1^{xy} \\ 0 & 0 & 0 & 0 & 1 & 0 & 0 \\ gh_f & 0 & 0 & -u_x^2+gh_f & 2u_x & 0 & gh_f \\ 0 & 0 & 0 & -u_xu_y & u_y & u_x & 0 \\ 0 & 0 & 0 & 0 & 0 & 0 & 0 \end{bmatrix} \quad (48)$$

and

$$B(W)=\begin{bmatrix} 0 & 0 & 1 & 0 & 0 & 0 & 0 \\ \frac{1}{2}(T_1^{xy}+T_2^{xy})-v_xv_y & v_y & v_x & \frac{1}{2}T_1^{xy} & 0 & 0 & T_1^{xy} \\ \frac{1}{2}(T_1^{yy}+T_2^{yy})-v_y^2+\rho gh_s & 0 & 2v_y & \frac{1}{2}T_1^{yy}+\rho gh_s & 0 & 0 & T_1^{yy}+\rho gh_s \\ 0 & 0 & 0 & 0 & 0 & 1 & 0 \\ 0 & 0 & 0 & -u_xu_y & u_y & u_x & 0 \\ gh_f & 0 & 0 & -u_y^2+gh_f & 0 & 2u_y & gh_f \\ 0 & 0 & 0 & 0 & 0 & 0 & 0 \end{bmatrix}, \quad (49)$$

with

$$T_1^{ij}=a_{ij}g(1-\rho)h_s, \quad T_2^{ij}=a_{ij}g(1-\rho)(h_s+h_f), \quad (50)$$

where i and j denote either x or y. According to Pelanti et al. [28] the Roe averages of the two-fluid model of Pitman and Le are given by

$$\tilde{h}_{s,f}=\frac{1}{2}\left(h_{s,f}^-+h_{s,f}^+\right), \quad \tilde{v}_{x,y}=\frac{\sqrt{h_s^-}v_{x,y}^-+\sqrt{h_s^+}v_{x,y}^+}{\sqrt{h_s^-}+\sqrt{h_s^+}},$$
$$\tilde{u}_{x,y}=\frac{\sqrt{h_f^-}u_{x,y}^-+\sqrt{h_f^+}u_{x,y}^+}{\sqrt{h_f^-}+\sqrt{h_f^+}}. \quad (51)$$

The source term $S(W)$ due to bottom drag and interphase friction is given by

$$S(W)=\begin{pmatrix} 0 \\ \rho Dh(u_x-v_x)-\frac{v_x}{|\vec{v}|}\tan(\Phi_b)g(1-\rho)h_s \\ \rho Dh(u_y-v_y)-\frac{v_y}{|\vec{v}|}\tan(\Phi_b)g(1-\rho)h_s \\ 0 \\ Dh(v_x-u_x) \\ Dh(v_y-u_y) \\ 0 \end{pmatrix}, \quad (52)$$

where the interphase drag function proposed by Pitman and Le [29] is used:

$$D=\frac{g}{v_T}\phi(1-\phi)^{1-m}\left(\frac{1}{\rho}-1\right). \quad (53)$$

The steady-state solution at rest for this system, neglecting the Coulomb friction term, is described by the following relations:

$$\phi = \frac{h_s}{h_s + h_f} = const., \quad \eta = h_s + h_f + b = const.,$$
$$u_x = u_y = v_x = v_y = 0, \tag{54}$$

and in terms of the jumps

$$(\phi - 1)\Delta h_s + \phi \Delta h_f = 0, \quad \Delta h_s + \Delta h_f + \Delta b = 0. \tag{55}$$

For the Pitman and Le model it is possible to show that the use of reconstruction in *characteristic variables* automatically leads to an exactly well-balanced scheme, since for the water at rest solution the characteristic variables are η and b.

It can be verified that using the following "well-balanced" identity matrix $\underline{\underline{I}}^{\mathrm{WB}}$ instead of $\underline{\underline{I}}$, the non-conservative Rusanov-type schemes will conserve exactly the steady-state solution (54), (55) at rest, where we use the notation $\hat{\phi} = 1 - \tilde{\phi}$ and $\tilde{\phi} = \frac{1}{2}(\phi^- + \phi^+)$:

$$\underline{\underline{I}}^{\mathrm{WB}} = \begin{pmatrix} 1 & 0 & 0 & 0 & 0 & 0 & \tilde{\phi} \\ 0 & 1 & 0 & 0 & 0 & 0 & 0 \\ 0 & 0 & 1 & 0 & 0 & 0 & 0 \\ 0 & 0 & 0 & 1 & 0 & 0 & \hat{\phi} \\ 0 & 0 & 0 & 0 & 1 & 0 & 0 \\ 0 & 0 & 0 & 0 & 0 & 1 & 0 \\ 0 & 0 & 0 & 0 & 0 & 0 & 0 \end{pmatrix}. \tag{56}$$

We note that the proposed matrix $\underline{\underline{I}}^{\mathrm{WB}}$ has a full set of linearly independent eigenvectors, four times the eigenvalue 1 and one zero eigenvalue 0, which corresponds to the eigenvector associated to the variable bottom b.

4. Numerical convergence studies

To our knowledge, no *unsteady multi-dimensional* test case with *exact* solution has been published so far for the two-layer shallow water equations or for the two-fluid flow model of Pitman and Le. All convergence test cases presented in [32,8] are steady and one-dimensional and in [28] no numerical convergence studies are shown. In this section we therefore introduce a new set of *unsteady* two-dimensional test cases with a simple analytical *exact* solution for the two-layer shallow water equations and for the two-fluid flow model of Pitman and Le. This allows us to verify the high order of accuracy of the numerical methods proposed in Section 2. The underlying idea for these new test cases is taken from the isentropic vortex test cases used in [20,1] to show convergence of numerical methods for the two-dimensional Euler and MHD equations, respectively. The exact solution of these unsteady test cases is obtained in two steps. First, one finds an exact stationary and rotationally symmetric solution of the governing PDE system (with $S(W) = 0$), that approaches a constant state as $r \to \infty$, in order to be compatible with periodic boundary conditions. Second, to make the test case unsteady, one uses the principle of Galilean invariance inherent in all governing equations based on Newtonian mechanics and superimposes a uniform velocity field to the solution found in step one. After one advection period through a periodic rectangular computational domain, the exact solution is then given by the initial condition.

4.1. Two-layer shallow water equations

After imposing rotational symmetry $\left(\frac{\partial}{\partial \theta} = 0\right)$, the steady two-layer shallow water equations in cylindrical coordinates $(r - \theta)$ read as follows:

$$\begin{aligned} g h_1 \frac{\partial}{\partial r}(h_1 + h_2) &= \frac{(v_1^\theta)^2 h_1}{r}, \\ g h_2 \frac{\partial}{\partial r}(h_2 + \rho h_1) &= \frac{(v_2^\theta)^2 h_2}{r}, \end{aligned} \tag{57}$$

where v_i^θ denote the velocities in angular (θ) direction and $\rho = \frac{\rho_1}{\rho_2} < 1$ denotes the density ratio between fluid 1 and fluid 2. We now prescribe a distribution for the velocities in angular direction that veri-

Table 1
Numerical convergence study of $P_N P_M$ schemes from second to sixth order of accuracy in space and time applied to the two-layer shallow water equations. Errors are shown for variable h_1.

N_G	L^2	$\mathcal{O}_{L^2}$	L^2	$\mathcal{O}_{L^2}$	L^2	$\mathcal{O}_{L^2}$ L^2	$\mathcal{O}_{L^2}$	L^2	$\mathcal{O}_{L^2}$	L^2	$\mathcal{O}_{L^2}$	
$\mathcal{O}2$	P_0P_1		P_1P_1									
64/24	2.24E − 02		3.41E − 02									
128/48	6.53E − 03	1.8	6.95E − 03	2.3								
192/64	2.83E − 03	2.1	3.81E − 03	2.1								
256/128	1.64E − 03	1.9	7.88E − 04	2.3								
$\mathcal{O}3$	P_0P_2		P_1P_2		P_2P_2							
32/16	5.80E − 02		2.74E − 02		8.54E − 03							
64/24	9.46E − 03	2.6	7.75E − 03	3.1	2.19E − 03	3.4						
128/32	1.41E − 03	2.7	2.49E − 03	3.9	8.08E − 04	3.5						
192/64	4.37E − 04	2.9	1.87E − 04	3.7	8.68E − 05	3.2						
$\mathcal{O}4$	P_0P_3		P_1P_3		P_2P_3		P_3P_3					
32/16	1.49E − 02		2.33E − 02		4.17E − 03		1.03E − 03					
64/24	1.04E − 03	3.8	6.46E − 03	3.2	5.52E − 04	5.0	1.78E − 04	4.3				
128/32	6.24E − 05	4.1	1.97E − 03	4.1	1.38E − 04	4.8	5.20E − 05	4.3				
192/64	1.17E − 05	4.1	9.65E − 05	4.4	6.83E − 06	4.3	3.06E − 06	4.1				
$\mathcal{O}5$	P_0P_4		P_1P_4		P_2P_4		P_3P_4		P_4P_4			
32/16	1.68E − 02		1.23E − 02		1.41E − 03		4.80E − 04		1.10E − 04			
64/24	1.10E − 03	3.9	1.56E − 03	5.1	1.46E − 04	5.6	4.63E − 05	5.8	1.10E − 05	5.7		
128/32	4.03E − 05	4.8	2.92E − 04	5.8	2.76E − 05	5.8	9.10E − 06	5.7	2.21E − 06	5.6		
192/64	5.59E − 06	4.9	4.83E − 06	5.9	9.04E − 07	4.9	3.22E − 07	4.8	1.79E − 07	3.6		
$\mathcal{O}6$	P_0P_5		P_1P_5		P_2P_5		P_3P_5		P_4P_5		P_5P_5	
32/ 8	7.58E − 03		5.67E − 02		3.00E − 02		9.84E − 03		3.58E − 03		1.20E − 03	
64/16	1.42E − 04	5.7	1.11E − 02	2.4	1.08E − 03	4.8	1.44E − 04	6.1	3.94E − 05	6.5	1.26E − 05	6.6
128/24	2.37E − 06	5.9	1.18E − 03	5.5	7.50E − 05	6.6	1.23E − 05	6.1	3.38E − 06	6.1	1.20E − 06	5.8
192/32	2.61E − 07	5.4	1.91E − 04	6.3	1.17E − 05	6.5	1.83E − 06	6.6	5.97E − 07	6.0	2.44E − 07	5.5

Table 2
Numerical convergence study of $P_N P_M$ schemes from second to sixth order of accuracy in space and time applied to the two-fluid model of Pitman and Le. Errors are shown for variable h_s.

N_G	L^2	$\mathcal{O}_{L^2}$	L^2	$\mathcal{O}_{L^2}$	L^2	$\mathcal{O}_{L^2}L^2$	$\mathcal{O}_{L^2}$	L^2	$\mathcal{O}_{L^2}$	L^2	$\mathcal{O}_{L^2}$	
$\mathcal{O}2$	P_0P_1		P_1P_1									
64/24	3.34E − 02		5.39E − 02									
128/48	9.51E − 03	1.8	1.14E − 02	2.2								
192/64	4.08E − 03	2.1	6.35E − 03	2.0								
256/128	2.45E − 03	1.8	1.27E − 03	2.3								
$\mathcal{O}3$	P_0P_2		P_1P_2		P_2P_2							
32/16	7.12E − 02		6.98E − 02		1.96E − 02							
64/24	1.96E − 02	1.9	1.67E − 02	3.5	4.75E − 03	3.5						
128/32	2.98E − 03	2.7	5.02E − 03	4.2	1.68E − 03	3.6						
192/64	9.18E − 04	2.9	2.91E − 04	4.1	1.75E − 04	3.3						
$\mathcal{O}4$	P_0P_3		P_1P_3		P_2P_3		P_3P_3					
32/16	3.20E − 02		6.31E − 02		9.16E − 03		2.12E − 03					
64/24	2.07E − 03	3.9	1.47E − 02	3.6	1.12E − 03	5.2	3.54E − 04	4.4				
128/32	1.28E − 04	4.0	4.35E − 03	4.2	2.56E − 04	5.1	1.02E − 04	4.3				
192/64	2.35E − 05	4.2	2.05E − 04	4.4	1.05E − 05	4.6	5.91E − 06	4.1				
$\mathcal{O}5$	P_0P_4		P_1P_4		P_2P_4		P_3P_4		P_4P_4			
32/16	4.56E − 02		3.13E − 02		2.77E − 03		9.47E − 04		2.45E − 04			
64/24	2.54E − 03	4.2	3.48E − 03	5.4	2.65E − 04	5.8	8.54E − 05	5.9	2.43E − 05	5.7		
128/32	8.88E − 05	4.8	6.31E − 04	5.9	4.92E − 05	5.8	1.71E − 05	5.6	4.79E − 06	5.6		
192/64	1.24E − 05	4.9	1.01E − 05	6.0	1.35E − 06	5.2	5.40E − 07	5.0	1.70E − 07	4.8		
$\mathcal{O}6$	P_0P_5		P_1P_5		P_2P_5		P_3P_5		P_4P_5		P_5P_5	
32/ 8	1.74E − 02		1.25E − 01		9.24E − 02		2.74E − 02		8.27E − 03		2.47E − 03	
64/16	2.97E − 04	5.9	2.73E − 02	2.2	2.28E − 03	5.3	2.64E − 04	6.7	7.40E − 05	6.8	2.55E − 05	6.6
128/24	5.14E − 06	5.9	2.59E − 03	5.8	1.61E − 04	6.5	1.88E − 05	6.5	5.78E − 06	6.3	2.68E − 06	5.6
192/32	4.43E − 07	6.0	4.11E − 04	6.4	2.39E − 05	6.6	2.90E − 06	6.5	1.02E − 06	6.0	4.90E − 07	5.9

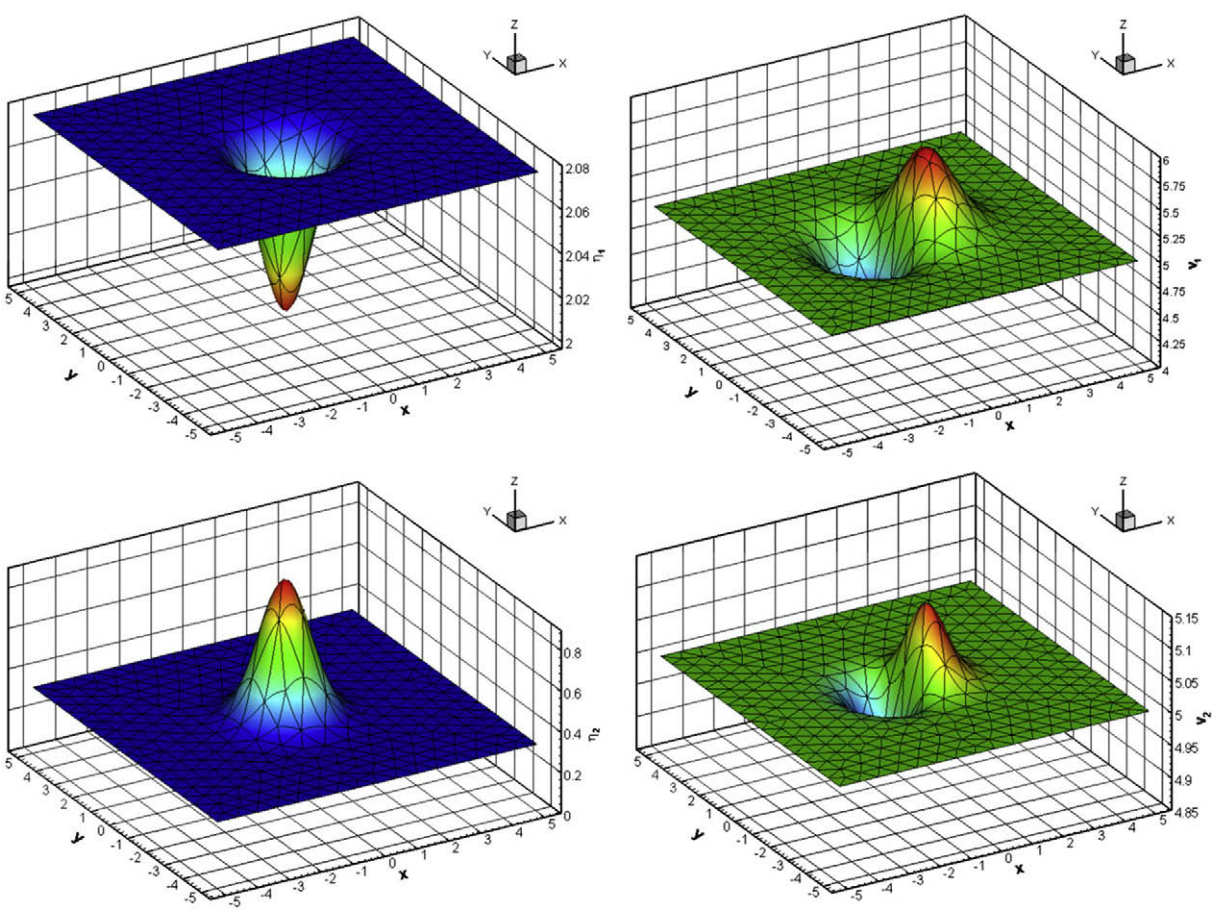

Fig. 1. Visualization of the numerical solution of the convergence test problem for the two-layer shallow water equations obtained with a sixth order discontinuous Galerkin scheme (P_5P_5) on the triangular mesh with $N_G = 16$ at $t = 2$.

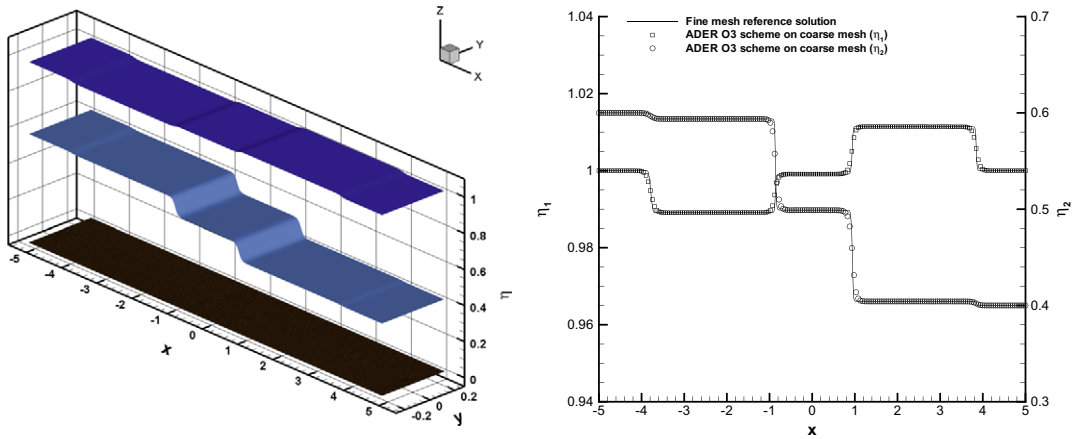

Fig. 2. (left) Numerical solution for the internal dam break problem with flat bottom obtained on a triangular mesh using a P_0P_2 ADER scheme. Results are shown for the free surface and the interface at time $t = 1.25$. (right) a cut along the x-axis is shown at $t = 1.25$, together with the 1D reference solution computed on 1000 elements.

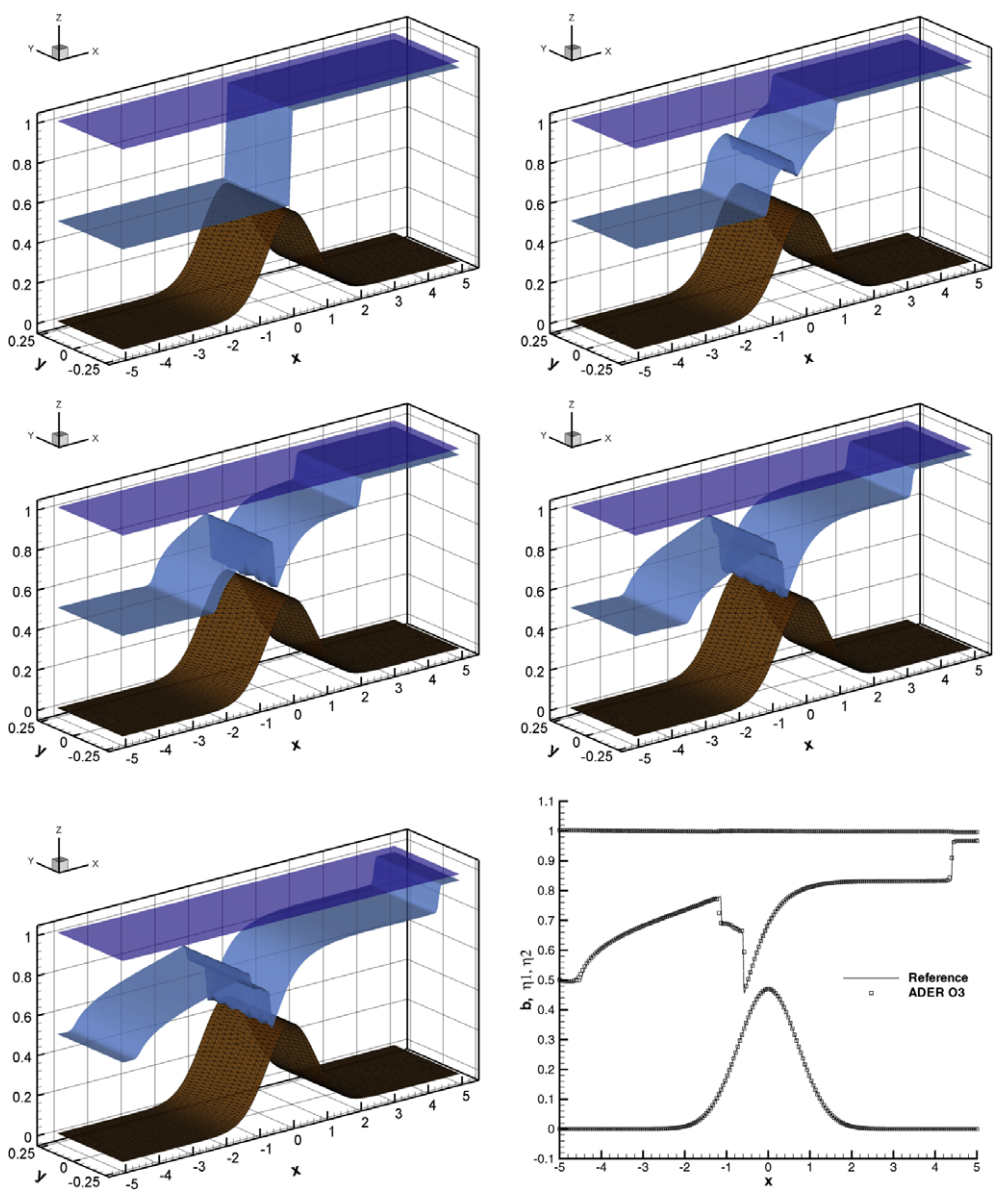

Fig. 3. Numerical solution and triangular mesh used for the lock exchange test case in a channel with variable bottom topography. Results at time $t = 0,\ t = 5,\ t = 10,\ t = 15$ and $t = 20$. In the bottom right figure, a cut along the x-axis is shown at $t = 20$, together with the 1D reference solution computed on 1000 elements.

fies the compatibility condition mentioned above. It is easily checked that the following functions satisfy $v_i^\theta \to 0$ for $r \to \infty$:

$$v_i^\theta = r v_{i0} e^{s_i(1-r^2)}. \tag{58}$$

To solve Eq. (57) we still need to specify appropriate boundary conditions for the unknowns h_1 and h_2. We choose the boundary conditions $h_1(0) = h_{10}$ and $h_2(0) = h_{20}$. With these boundary conditions the nonlinear ODE system (57) has the following solution for $H_1 := h_1(r)$ and $H_2 := h_2(r)$, which also satisfies the compatibility condition for $r \to \infty$:

$$\begin{aligned} H_1 &= \frac{1}{4}\frac{v_{10}^2 s_2 e^{2s_1}(1-e^{-2s_1 r^2}) - v_{20}^2 s_1 e^{2s_2}(1-e^{-2s_2 r^2}) + 4h_{10} g s_1 s_2 (1-\rho)}{g(1-\rho)s_1 s_2}, \\ H_2 &= \frac{1}{4}\frac{v_{20}^2 s_1 e^{2s_2}(1-e^{-2s_2 r^2}) - \rho v_{10}^2 s_2 e^{2s_1}(1-e^{-2s_1 r^2}) + 4h_{20} g s_1 s_2 (1-\rho)}{g(1-\rho)s_1 s_2}. \end{aligned} \tag{59}$$

After having found the steady rotationally symmetric solution of the PDE, we can superimpose a uniform velocity field $\vec{v} = (\bar{u}, \bar{v})^T$ to obtain the following initial condition for the proposed *unsteady* test case:

$$\begin{aligned} &(h_1, u_1, v_1, h_2, u_2, v_2, b) = \big(H_1, \bar{u} - v_1^\theta \sin(\theta), \bar{v} + v_1^\theta \cos(\theta), \\ &H_2, \bar{u} - v_2^\theta \sin(\theta), \bar{v} + v_2^\theta \cos(\theta), 0\big). \end{aligned} \tag{60}$$

Note that $x = r\cos(\theta)$ and $y = r\sin(\theta)$ to convert cylindrical to Cartesian coordinates. We solve the two-layer shallow water equations given by Eqs. (2) and (42), (43) with the initial condition (60) on the computational domain $\Omega = [-5;5] \times [-5;5]$ with four periodic boundary conditions. The gravity constant is set to $g = 10$ and for the density ratio we use $\rho = \frac{9}{10}$. For the other parameters we choose:

$$\begin{aligned} &s_1 = \frac{1}{2}, \quad s_2 = 1, \quad v_{10} = \frac{3}{4}, \quad v_{20} = \frac{1}{10}, \quad h_{10} = 1, \\ &h_{20} = 1, \quad \bar{u} = \bar{v} = 5. \end{aligned} \tag{61}$$

After one advection period ($T = 2$) the exact solution is given by the initial condition. The results are shown in Table 1. We emphasize that due to the finite computational domain, the compatibility condition at the boundaries is not satisfied exactly. This produces small jumps in the velocity field at the periodic boundaries, which can be detected in a numerical convergence study by a drop in the order of accuracy on sufficiently refined meshes. We detect such an accuracy drop at and below L_2 errors of the order 10^{-7}. If one wanted to fulfill the compatibility conditions better, one would simply have to enlarge the computational domain or one would have to increase the parameters s_1 and s_2, making the test case, however, more difficult since the spatial scales thus become smaller compared to the length scale of Ω. The results of the numerical convergence study are presented for all possible $P_N P_M$ schemes from second to sixth order of accuracy in space and time. The Courant number with respect to the one-dimensional stability limits given in [12] has been set to 0.5 in all cases presented in this paper. In contrast to the conservative case presented in [12], where the intermediate $P_N P_M$ schemes have been more efficient than pure DG or pure FV schemes in terms of computational effort, in the non-conservative case treated in this article, the pure DG schemes definitely seem to be the most efficient schemes in terms of accuracy and number of degrees of freedom compared to intermediate $P_N P_M$ schemes or pure finite volume methods.

4.2. The two-fluid flow model of Pitman and Le

Using again rotational symmetry ($\frac{\partial}{\partial\theta} = 0$), the steady frictionless ($v_T = \infty, \Phi_b = 0$) two-fluid flow model of Pitman and Le in cylindrical coordinates (r–θ) reads as follows:

$$\begin{aligned} &g h_s \frac{\partial}{\partial r}\left(h_s + \frac{1+\rho}{2} h_f\right) + \frac{1-\rho}{2} g h_f \frac{\partial}{\partial r} h_s = \frac{(v_s^\theta)^2 h_s}{r}, \\ &g h_f \frac{\partial}{\partial r}(h_s + h_f) = \frac{(v_f^\theta)^2 h_f}{r}, \end{aligned} \tag{62}$$

where v_i^θ are again the velocities in angular direction and $\rho = \frac{\rho_f}{\rho_s} < 1$ denotes the density ratio between the fluid and the solid. Since we were not able to find a general solution of the nonlinear ODE system (62), we proceed in the following way: We use the solution (59) of the two-layer shallow water equations for the depths $h_s(r) = H_1$ and $h_f(r) = H_2$ in order to get physically reasonable non-negative values for the depths h_s and h_f. Then we solve (62) directly for the angular velocities v_s^θ and v_f^θ. The angular velocities are thus given by

$$v_f^\theta = r v_{10} e^{s_1(1-r^2)} \tag{63}$$

and

$$v_s^\theta = \sqrt{r g \frac{\partial}{\partial r}\left(H_1 + \frac{1+\rho}{2} H_2\right) + r \frac{1-\rho}{2} g \frac{H_2}{H_1} \frac{\partial}{\partial r} H_1}. \tag{64}$$

We run the same test case as for the two-layer shallow water equations, i.e. using the same computational domain Ω with the same parameters as given in (61). The results are shown in Table 2 (see Fig. 1).

5. Applications

5.1. The two-layer shallow water equations

5.1.1. Internal dam break

We solve an internal dam-break problem over a flat bottom topography ($b = 0$) using the two-layer shallow water equations

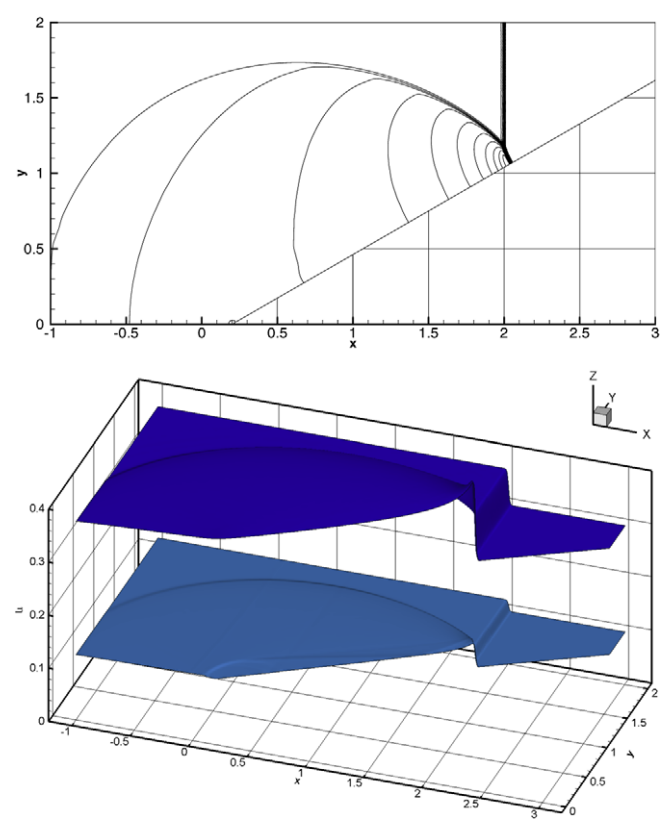

Fig. 4. Numerical solution for the wave reflection problem solving the two-layer shallow water equations. An isolated discontinuity, initially located at $x = 0$, is travelling to the right with speed $s = 2$ and hits a 30° ramp. 21 equidistant contourlines from 0.31 to 0.45 are shown for variable η_1 at time $t = 1$ (top). A 3D view of the solution is also shown (bottom).

in the two-dimensional computational domain $\Omega = [-5;5] \times [-0.25;0.25]$. The unstructured triangular mesh has 4424 triangles, corresponding to a one-dimensional resolution of the problem of 200 points, or a characteristic mesh spacing of $h = 0.05$. The initial condition is given by a discontinuity in h_1 and h_2, located at $x = 0$. The discharges of both layers are initially zero, i.e. $q_1(x,0) = q_2(x,0) = 0$, and the left and right states for the depth function h_1 are $h_1^L(x,0) = 0.4$ and $h_1^R(x,0) = 0.6$, respectively. The free surface height η is constant $\eta = 1$, so that $h_2^L = 0.6$ and $h_2^R = 0.4$. We use periodic boundaries in y-direction and transmissive boundaries in x-direction. We furthermore use $g = 9.81$ and $\rho = 0.8$. The computation is done with a third order P_0P_2 ADER WENO finite volume scheme as presented in this paper. The numerical solution obtained at $t = 1.25$ for η_1 and η_2 together with the triangular mesh are shown in Fig. 2. A 1D reference solution obtained on a fine mesh of 1000 points is compared against the unstructured 2D computation and shows a very good agreement.

5.1.2. Internal dam break problem with variable bottom topography

In contrast to the previous test with flat bottom, this test case now represents an internal dam-break problem with variable bottom topography and has been inspired from [10]. We solve the two-layer shallow water equations in the two-dimensional computational domain $\Omega = [-5;5] \times [-0.25;0.25]$ using an unstructured triangular mesh with 4424 triangles, corresponding to a one-dimensional resolution of the problem of 200 points, or a characteristic mesh spacing of $h = 0.05$. The bottom topography is defined by $b(x) = \left(\frac{1}{2} - \delta\right)e^{-x^2}$. The initial condition for the other variables is given by a discontinuity located at $x = 0$. The discharges of both layers are zero, i.e. $q_1(x,0) = q_2(x,0) = 0$, and the left and right states for the depth function h_1 are $h_1^L(x,0) = 0.5$ and $h_1^R(x,0) = \delta$, respectively. The free surface height η is constant $\eta = 1$, so that $h_2(x,0) = \eta - h_1(x,0)$. For the parameter δ we choose $\delta = 0.03$. As boundary conditions we use periodic boundaries in y-direction and impose Dirichlet boundary conditions consistent with the initial condition at the left and right boundaries in x-direction. We furthermore use $g = 9.81$ and $\rho = 0.98$. The computation is done with a third order P_0P_2 ADER WENO finite volume scheme. The numerical solution obtained for b, η_1 and η_2 together with the triangular mesh are shown in Fig. 3. A 1D reference solution obtained on a fine mesh of 1000 points is compared against the unstructured 2D computation and shows an excellent agreement.

5.1.3. 2D wave reflection problem

This test case is an adaptation of the double Mach reflection problem, originally proposed by Woodward and Colella in [39], which is very popular in compressible gasdynamics. It consists of an isolated shock wave travelling to the right and hitting a 30° ramp. The computational domain Ω is shown in Fig. 4, where we set reflective wall boundary conditions on the upper and lower boundaries of the domain and Dirichlet boundary conditions on the left and right that correspond to the initial condition. To adapt the problem to our case of a non-conservative hyperbolic system, we choose a segment path connecting the left and right state of the discontinuity, initially located at $x = 0$ and moving with speed $s = 2$. The bottom is flat, $b = 0$. The right state (at rest) is chosen to be $h_1^R = 0.2$, $h_2^R = 0.1$ and $q_1^R = q_2^R = 0$. We furthermore set $g = 10$ and $\rho = 0.9$. Using the segment path, the velocity s of the discontinuity and the right state, we obtain the following left state, using

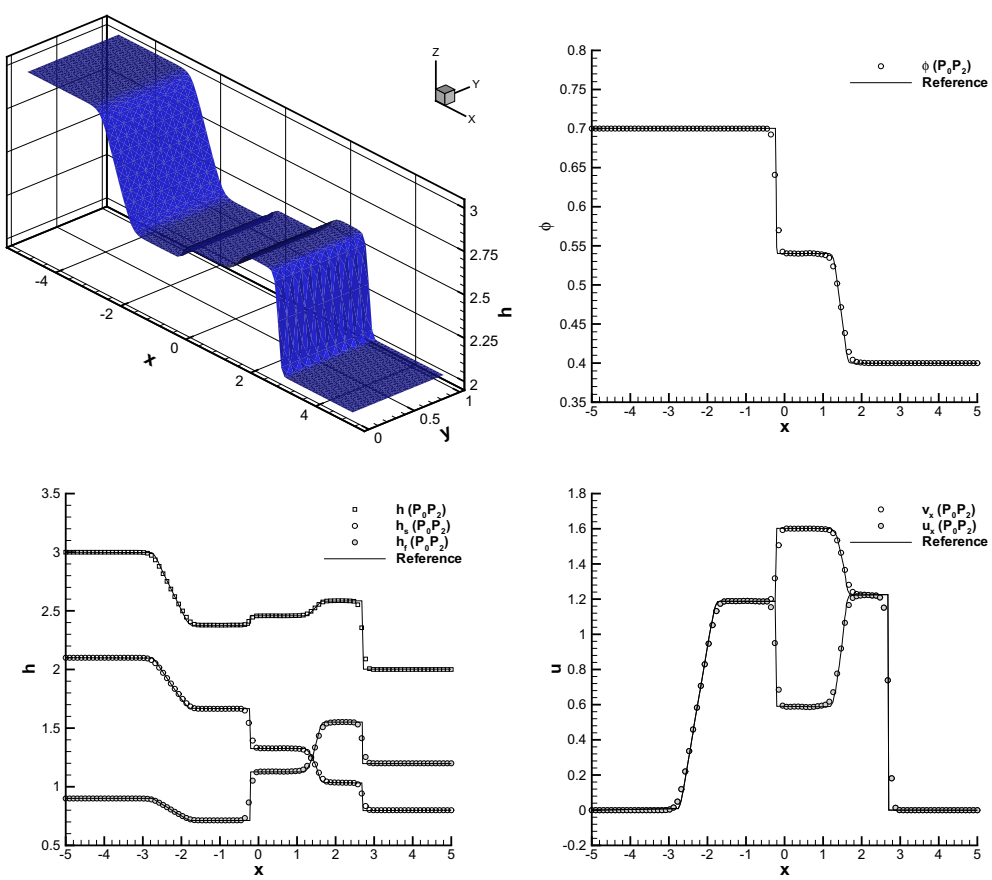

Fig. 5. Numerical solution at $t = 0.5$ and regular triangular mesh used for Riemann problem RP1 for the two-fluid model of Pitman and Le. The reference solution has been taken from [28].

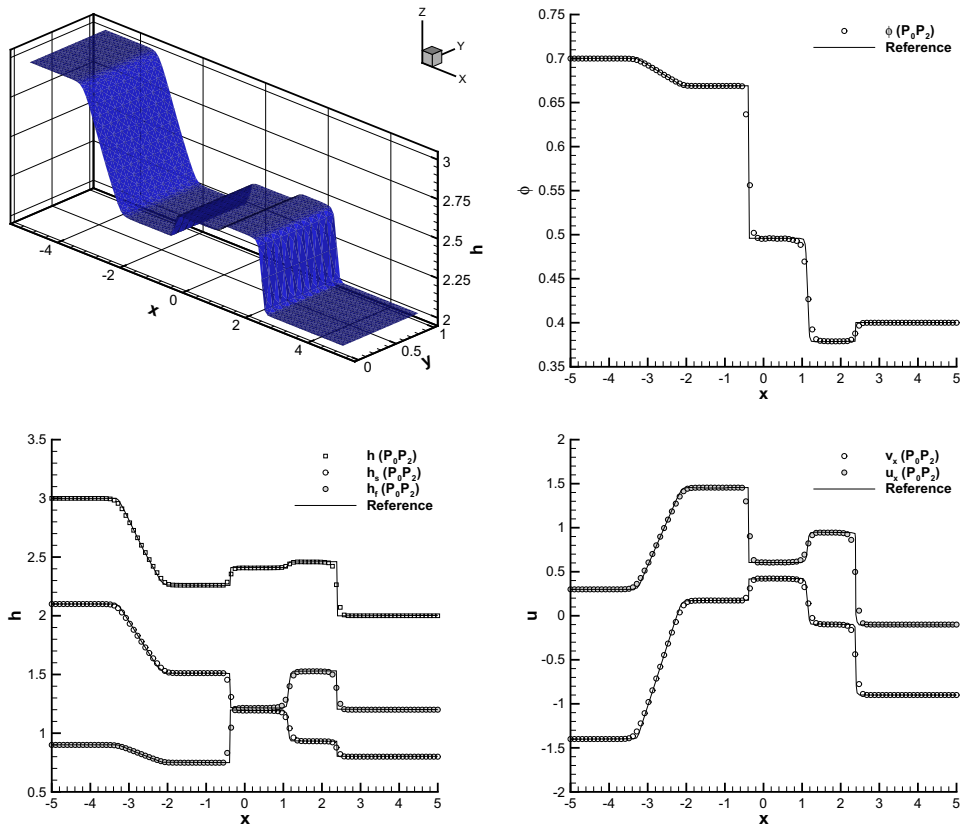

Fig. 6. Numerical solution and regular triangular mesh used for Riemann problem RP2 for the two-fluid model of Pitman and Le. The reference solution has been taken from [28].

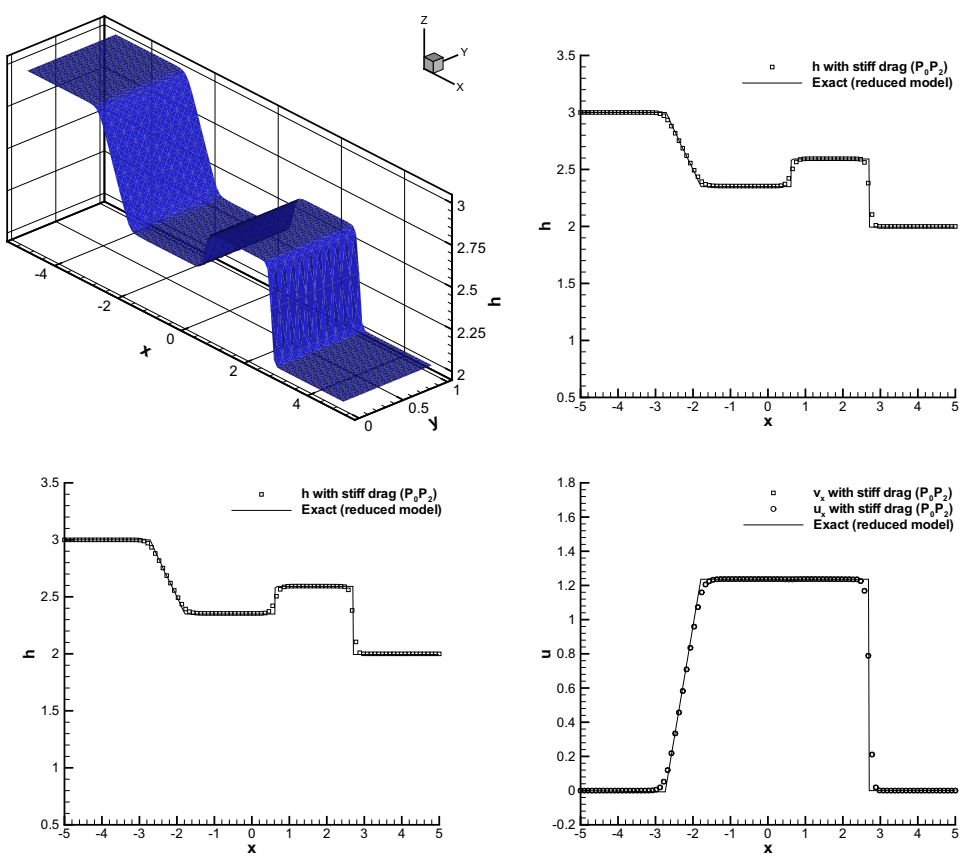

Fig. 7. Numerical solution and regular triangular mesh used for the stiff version of Riemann problem RP1 for the two-fluid model of Pitman and Le. The reference solution has been taken from [28].

symbolic algebra tools to solve the generalized Rankine–Hugoniot conditions (3): $h_1^L = 0.2466050571$, $q_1^L = 0.09321011423$, $h_2^L = 0.1211009827$ and $q_2^L = 0.04220196541$. We use a third order P_0P_2 WENO finite volume scheme on a triangular mesh with 129,808 triangles, corresponding to a characteristic mesh spacing of $h = 1/100$. In Fig. 4 one can easily check that the incident discontinuity moves with the correct velocity $s = 2$ since it travels from its initial position $x = 0$ to $x = 2$ at time $t = 1$. We refer to [9], where a detailed discussion is given that underlines that even using path-conservative schemes does not always guarantee a correct shock position for general non-conservative hyperbolic systems.

5.2. The two-fluid flow model of Pitman and Le

In this section we first solve a sequence of two-dimensional test problems originally proposed in one space dimension by Pelanti et al. in [28], from where the reference solutions have been taken using a digitizer software. From our point of view the procedure of comparing our 2D results against one-dimensional reference solutions obtained by other international research teams and obtained with different numerical methods – if available – seems more appropriate than just comparing our 2D results against fine-mesh results obtained with our own 1D method, in particular in the light of the recent results shown in [9], where the authors show that even formally path-consistent schemes may fail to converge for general non-conservative systems.

The regular triangular meshes used for the shock-tube problems in this section have been obtained from an initially Cartesian mesh where each square has been split into four triangles by connecting the corners of the square with its barycenter. Hence each of the resulting triangles has one edge that is aligned with one of the coordinate axes and two edges of the triangle are tilted with respect to both coordinate axes by 45°. The use of unstructured triangular meshes makes even these originally one-dimensional test cases two-dimensional. We underline that solving 1D Riemann problems on 2D meshes is a useful test in order to assess the accuracy and robustness of a numerical scheme, in particular for Roe-type methods, since it has been shown by Quirk [31] that one may obtain spurious shock wave instabilities, so-called carbuncle solutions [16], when using Roe's method in multiple space dimensions to solve one-dimensional shock-tube problems. The technique of solving 1D Riemann problems on 2D unstructured meshes to validate multi-dimensional WENO schemes on triangular meshes has first been adopted by Hu and Shu in [20].

5.2.1. Riemann problem RP1 without friction

The initial condition for this test problem with flat bottom ($b = 0$) is given by $u_x = u_y = v_x = v_y = 0$, and a discontinuity located at $x = 0$ with $h_L = 3$, $\phi_L = 0.7$, $h_R = 2$ and $\phi_R = 0.4$. We use $g = 9.8$, $\rho = 0.5$ and $\Phi_b = 0$. In our case we use a *two-dimensional* computational domain $\Omega = [-5; 5] \times [0; 1]$ with periodic boundaries in y-direction and transmissive boundaries in x-direction. A third order P_0P_2 WENO finite volume scheme is used. Our numerical results obtained on the 2D domain are shown in Fig. 5 and are compared with the reference solution provided by Pelanti et al. in [28] using a second order TVD finite volume method in one space dimension on a mesh containing 1000 points. We note an excellent agreement between our two-dimensional computation using a third order P_0P_2 WENO scheme on an unstructured triangular mesh with an equivalent one-dimensional resolution of 100 points and the one-dimensional reference solution. Despite the use of a third order accurate method, the solution remains visibly oscillation free due to the nonlinear WENO reconstruction operator.

5.2.2. Riemann problem RP2 without friction

The initial condition for this test problem with flat bottom ($b = 0$) exhibits relatively large differences in the phase velocities and is given again by a discontinuity located at $x = 0$ with $h_L = 3$, $\phi_L = 0.7$, $h_R = 2$ and $\phi_R = 0.4$. In addition, the phase velocities are now chosen to be $v_x^L = -1.4$, $u_x^L = 0.3$, $v_x^R = -0.9$ and $u_x^R = -0.1$. The velocities in y direction remain all zero. We use again $g = 9.8$, $\rho = 0.5$, $\Phi_b = 0$ and the same domain Ω as in the previous case. Also the boundary conditions and the numerical method are the same. The reference solution is again taken from [28]. The results are shown in Fig. 6. We again note the excellent agreement between our two-dimensional unstructured computation using a third order WENO method and the one-dimensional TVD finite volume reference solution. Our new path-conservative third order P_0P_2 WENO finite volume scheme accurately resolves the discontinuities, reproduces the right shock positions and produces no spurious oscillations.

5.2.3. Riemann problem RP1 with stiff friction

The parameters and the initial condition for this test problem are the same as for RP1. However, we now switch on a very stiff interphase drag term choosing $v_T = 10^{-6}$ and $m = 1$. The Coulomb bottom friction is still neglected in this test case, i.e. we set again $\Phi_b = 0$. Since the source term is stiff, we use the local *discontinuous* space–time Galerkin predictor in this computation. The time step of our globally explicit scheme is still chosen according to the CFL stability criterion (using a Courant number of 0.5) as $\Delta t = 3 \times 10^{-3}$. For a detailed discussion of the treatment of stiff source terms using the local space–time discontinuous Galerkin predictor method used in this paper see [13,11], where the method

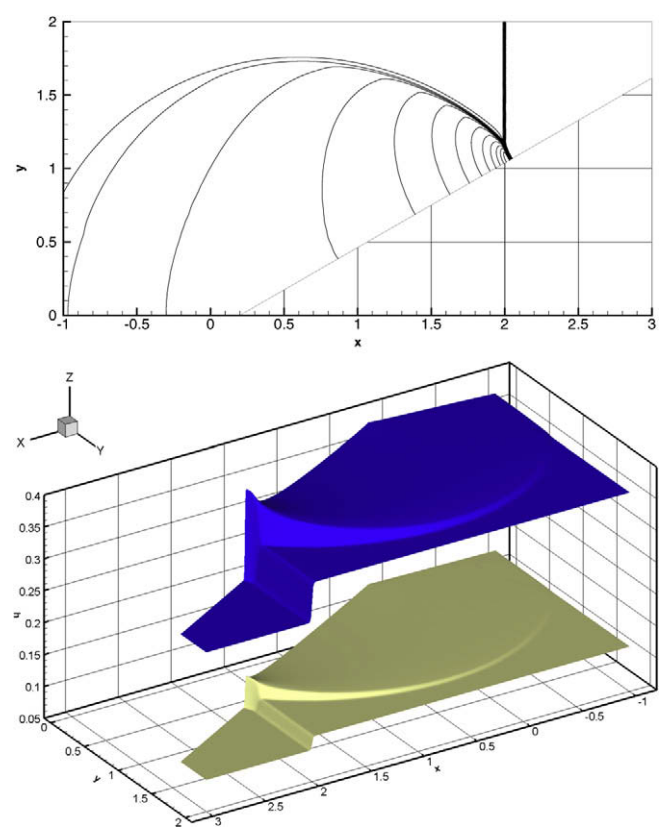

Fig. 8. Numerical solution for the wave reflection problem solving the Pitman and Le two-fluid model. An isolated discontinuity, initially located at $x = 0$, is travelling to the right with speed $s = 2$ and hits a 30° ramp. Twenty-one equidistant contourlines from 0.105 to 0.145 are shown for variable h_s at time $t = 1.0$ (top). A 3D view of the solution is shown on the bottom.

has shown to reach the optimal order of accuracy and to be also asymptotically consistent, in contrast to standard operator splitting schemes. For stiff interphase drag, Pelanti et al. derived a reduced model for which even an exact solution is available. We use again a third order P_0P_2 WENO finite volume scheme on the same domain Ω and the same unstructured triangular mesh as in the previous two test cases. The results are depicted in Fig. 7. This time, an exact reference solution is available. Also for this test problem we find an excellent agreement between our two-dimensional computation using a third order P_0P_2 WENO scheme on unstructured meshes and the exact reference solution, which has been derived from the reduced asymptotic model supposing instantaneous velocity relaxation to equilibrium. The discontinuities are all very-well resolved and at the right locations and no spurious oscillations are visible.

5.2.4. 2D wave reflection problem

This test case is similar to the one proposed in this paper for the two-layer shallow water equations. It consists again of an isolated shock wave travelling to the right and hitting a 30° ramp. The computational domain Ω is depicted in Fig. 8, where we set reflective wall boundary conditions on the upper and lower boundaries of the domain and Dirichlet boundary conditions on the left and right that correspond to the initial condition. We choose again a segment path connecting the left and right state of the discontinuity, initially located at $x = 0$ and moving with speed $s = 2$. The bottom is flat, $b = 0$. The right state (at rest) is chosen to be $h_s^R = 0.1$, $h_f^R = 0.2$ and all velocities on the right are zero. We furthermore set $g = 10$ and $\rho = 0.5$. No friction terms are present, i.e. $\Phi_b = 0$ and $v_T = \infty$. Using the segment path, the velocity s of the discontinuity and the right state, we obtain the following left state, using symbolic algebra tools to solve the resulting Rankine–Hugoniot conditions (3): $h_s^L = 0.1207825128$, $h_s v_x^L = 0.04156502553$, $h_f^L = 0.2415650255$ and $h_f u_x^L = 0.08313005106$. We use a third order P_0P_2 WENO finite volume scheme on a triangular mesh with 129,808 triangles, corresponding to a typical mesh spacing of $h = 1/100$. In Fig. 8 on can easily check that the incident discontinuity moves with the correct velocity $s = 2$, since it travels from its initial position $x = 0$ to $x = 2$ at time $t = 1$.

5.2.5. Small perturbation of a steady solution at rest

This test case is a modification of the well-known test problem introduced by Leveque for the single layer shallow water equations in [22] and was first proposed by Pelanti et al. in [28] for the Pitman and Le model. The bottom topography is defined by

$$b(x) = \begin{cases} 0.25\left(\cos\left(10\pi\left(x - \frac{1}{2}\right)\right) + 1\right) & \text{if } |x - 0.5| < 0.1, \\ 0 & \text{else.} \end{cases} \tag{65}$$

All velocities are zero and a small perturbation is added to the flow depth h and the solid volume fraction ϕ:

$$h(x,0) = h_0 + \delta h, \quad \phi(x,0) = \phi_0 - \delta\phi \qquad \text{for } -0.6 < x < -0.5. \tag{66}$$

We use $h_0 = 1$, $\phi_0 = 0.6$ and $\delta h = \delta\phi = 10^{-3}$. In addition, for this test case, $g = 1$, $\Phi_b = 0$ and $\rho = 0.5$ are used. We choose the following computational domain $\Omega = [-1.2; 1.1] \times [0; 0.2]$, which is slightly larger in x-direction than the one chosen in [28]. The mesh consists of 4800 triangles with a characteristic mesh spacing of $h = \frac{1}{50}$. This test case is used to illustrate the well-balancedness of the underlying numerical scheme and is very difficult for those schemes which are not exactly well-balanced. A 3D display of the solution is shown in Fig. 9 and a cut along the x-axis is depicted in Fig. 10. An excellent agreement with the 1D reference solution can be observed and we underline furthermore that our proposed scheme does not produce spurious oscillations due to the variable bottom topography.

5.2.6. A Debris flow problem in complex geometry

This final application aims at showing the *potential* of our proposed high order accurate numerical method on unstructured meshes for non-conservative hyperbolic systems. We propose a debris flow problem in a complex geometry, as it may be of interest for geoscientists, civil or environmental engineers. We emphasize that a main feature of our proposed schemes is that they run on unstructured triangular meshes which allow for an entirely automatic mesh generation even in highly complex geometries by the use of modern mesh generator software. We solve the two-fluid debris flow model of Pitman and Le. A sketch of the computational domain Ω is depicted in Fig. 11 and consists of the following three parts:

- a rectangular domain $[-2; 2] \times [-2.5; 2.5]$,
- a convergent–divergent channel, whose geometry is given by two cosine functions $y = \pm(1.75 + A\cos(2\pi/\lambda \cdot (x - 2)))$ with wavelength $\lambda = 10$ and wave amplitude $A = 0.75$,
- a square domain $[12; 32] \times [-10; 10]$ with a cut-out unit circle, whose center is located at the position $\vec{x}_c = (16, 0)$. This models for example a cylindrical pillar that is subject to the impact of the incident debris flow.

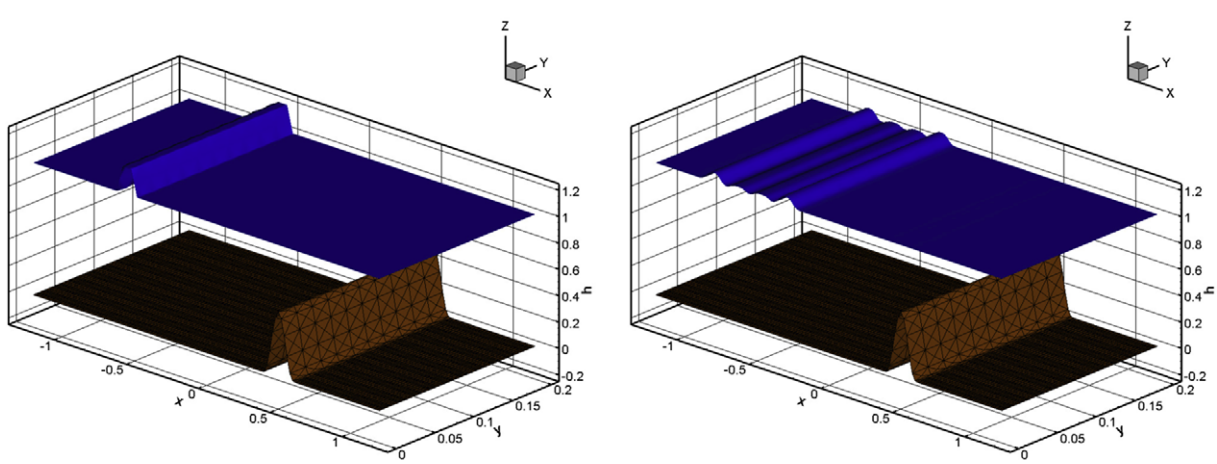

Fig. 9. Small perturbation of a steady-state solution with variable bottom topography. 3D view of the results at times $t = 0$ and $t = 0.25$. The solution of the free surface η is amplified to make the perturbation visible. No spurious perturbations of the surface due to the bottom topography are present.

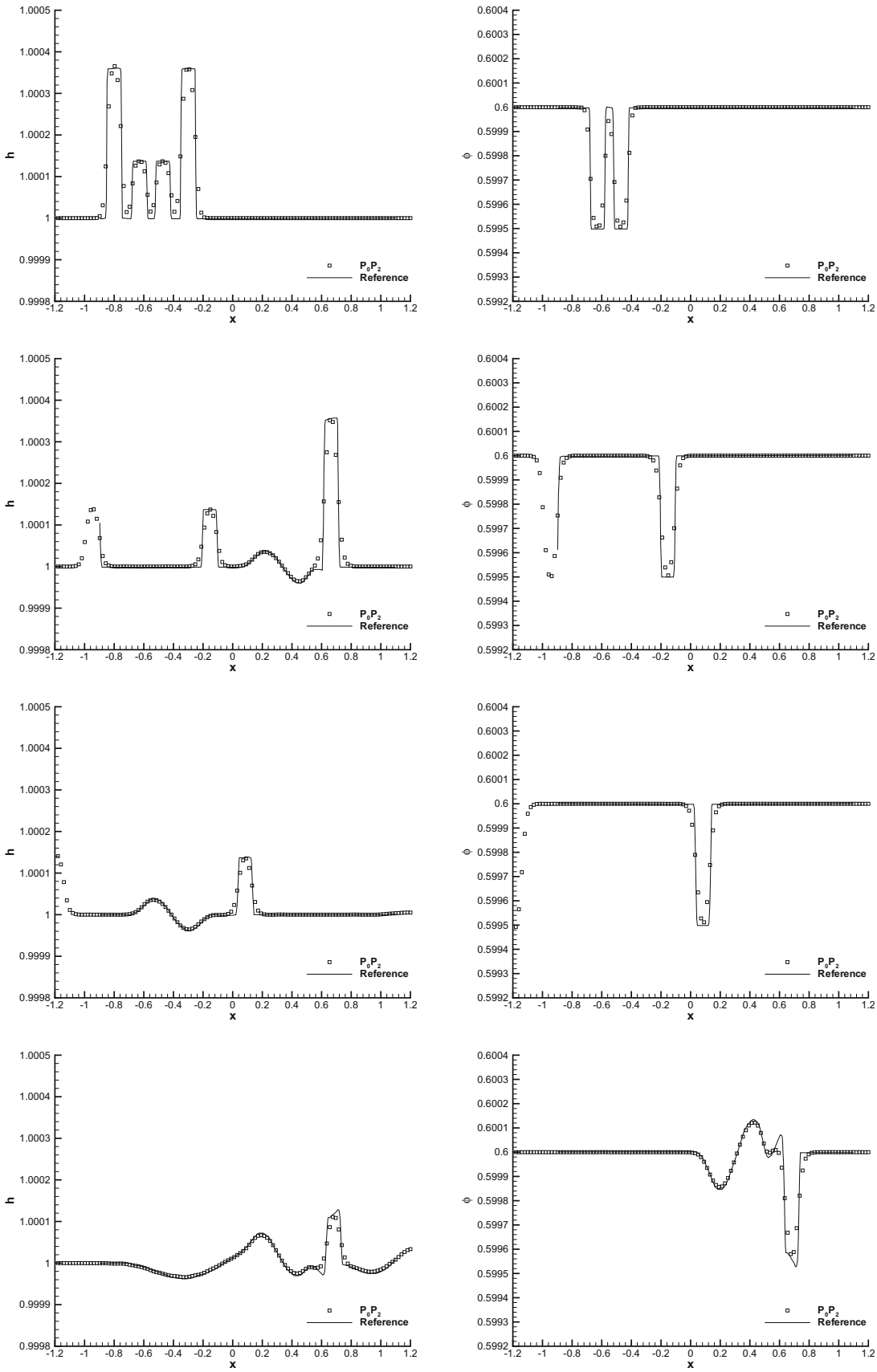

Fig. 10. Small perturbation of a steady-state solution with variable bottom topography. Results for total depth h (left column) and solid volume fraction ϕ (right column) at times $t = 0.25,\ t = 1.25,\ t = 2.0$ and $t = 4.0$ computed with a P_0P_2 WENO scheme using the Pitman and Le model. The reference solution has been taken from [28].

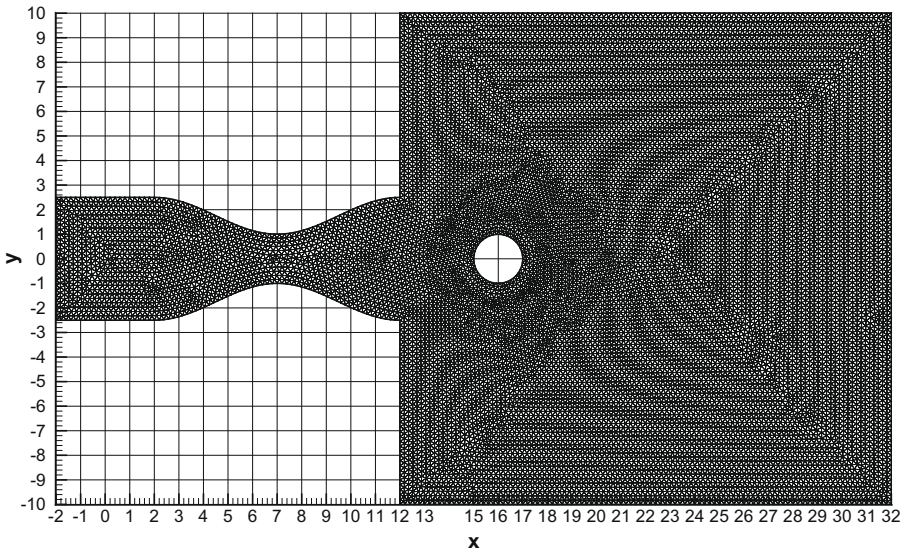

Fig. 11. Computational domain Ω and coarse triangular mesh for the realistic debris flow problem.

The bottom topography b is given by the following function:

$$b(x,y) = \begin{cases} 2.5 & \text{if } x < 0, \\ 2.5 - 0.25x & \text{if } 0 < x < 10, \\ 0 & \text{otherwise}. \end{cases} \tag{67}$$

The mesh consists of 27,580 triangles with a mesh spacing of $h = 0.2$. Initially, the solid volume fraction is $\phi = 0.5$ everywhere. The depth h is set to $h = 0.01$ in the whole computational domain in order to avoid wetting and drying, whose proper treatment is not the scope of this article. We set $h = 4 - b(x)$ in the zone $-2 \leqslant x \leqslant 2$. All velocities are initially zero. We furthermore use the following parameters for our simulation: $g = 9.8$, $\rho = 0.5$, $\upsilon_T = 2$, $m = 0$ and $\Phi_b = 28^\circ$. We impose reflective wall boundary conditions on *all* boundaries of the computational domain in order to obtain a closed system. The numerical solution is obtained using a third order accurate P_0P_2 ADER WENO scheme as presented in this article. A three-dimensional view of our results is shown in Fig. 12, where the z-axis is magnified by a factor of 4 in order to make the structures of the flow more visible. On the z-axis we visualize at the same time the bottom topography b (in brown) and the total free surface $\eta = h + b$ using the variable ϕ for the colorcode. We observe that in the first instants of the debris flow phenomenon, the solid volume fraction remains almost unchanged and only at the tip of the flow we have more water than solid. This can be explained by the fact that the Coulomb friction exerts a resistive force on the solid phase, but none on the liquid phase, which is almost free to flow downwards. However, due to the choice $\upsilon_T = 2$, there is still a strong friction between the two phases so that the movement of the liquid and solid phase are not completely decoupled. At times $t = 1$, $t = 2$ and $t = 3$ we observe that the flow is reflected from the solid walls of the convergent–divergent channel and that in the nozzle a shock wave is formed that travels upstream. From $t = 2$ on we see the impact of the debris flow against the pillar and the wave reflections and refractions that are generated around the obstacle. From $t = 5$ onwards we can observe that the main flow is coming to a halt and that the material in the channel is drying out since the solid phase is held back by the Coulomb friction and the liquid phase slowly moves down the slope, decelerated by the interphase friction. At time $t = 25$ the system has almost reached its steady-state equilibrium, with an almost dry region at the channel, a deposit of liquid and solid phase around the circular obstacle and a region away from the deposits that contains almost only water.

6. Summary and conclusions

In this article we have introduced a new family of high order accurate finite volume and discontinuous Galerkin finite element schemes on unstructured meshes for the solution of non-conservative hyperbolic systems in multiple space dimensions. We use the general P_NP_M framework presented in [12], which unifies finite volume and discontinuous Galerkin methods in a more general class of schemes. Monotonicity of the finite volume method is assured via a WENO reconstruction operator [14,15]. The construction of a limiter for the general P_NP_M schemes is still work in progress. Our method is also able to deal with stiff algebraic source terms using a local space–time discontinuous Galerkin predictor method [13] that evolves the reconstructed polynomial data inside each element during one time step. The jumps across the element interfaces are treated exactly as in the high order accurate path-conservative Roe-type finite volume schemes of Parés [26] and Castro et al. [8], which are consistent with the theory of Dal Maso, LeFloch and Murat [23]. It has been proven that the proposed path-conservative P_NP_M schemes reduce to the classical conservative P_NP_M formulation in the case where the PDE system (2) is a conservation law (1), i.e. when the system matrices A, B and C are the Jacobians of some flux functions f, g and h, respectively.

We have shown numerical convergence studies of our schemes from second to sixth order of accuracy in space and time on two unsteady two-dimensional test cases for the two-layer shallow water equations and the two-fluid flow model of Pitman and Le. For this purpose, we have derived new analytical solutions of the governing equations. We have also shown the well-balancedness of the proposed numerical schemes using a modified version of the test problem of LeVeque [22] and some classical internal dam break problems. Finally, we have presented wave-impact problems against an inclined wall and a more realistic debris flow test problem in a rather complex geometry.

Future work will concern the extension of the present path-conservative P_NP_M schemes on unstructured meshes to compressible multi phase flow problems, since many existing mathematical models, such as the well-known Baer–Nunziato equations, contain non-conservative products. An apparent disadvantage of the Roe-

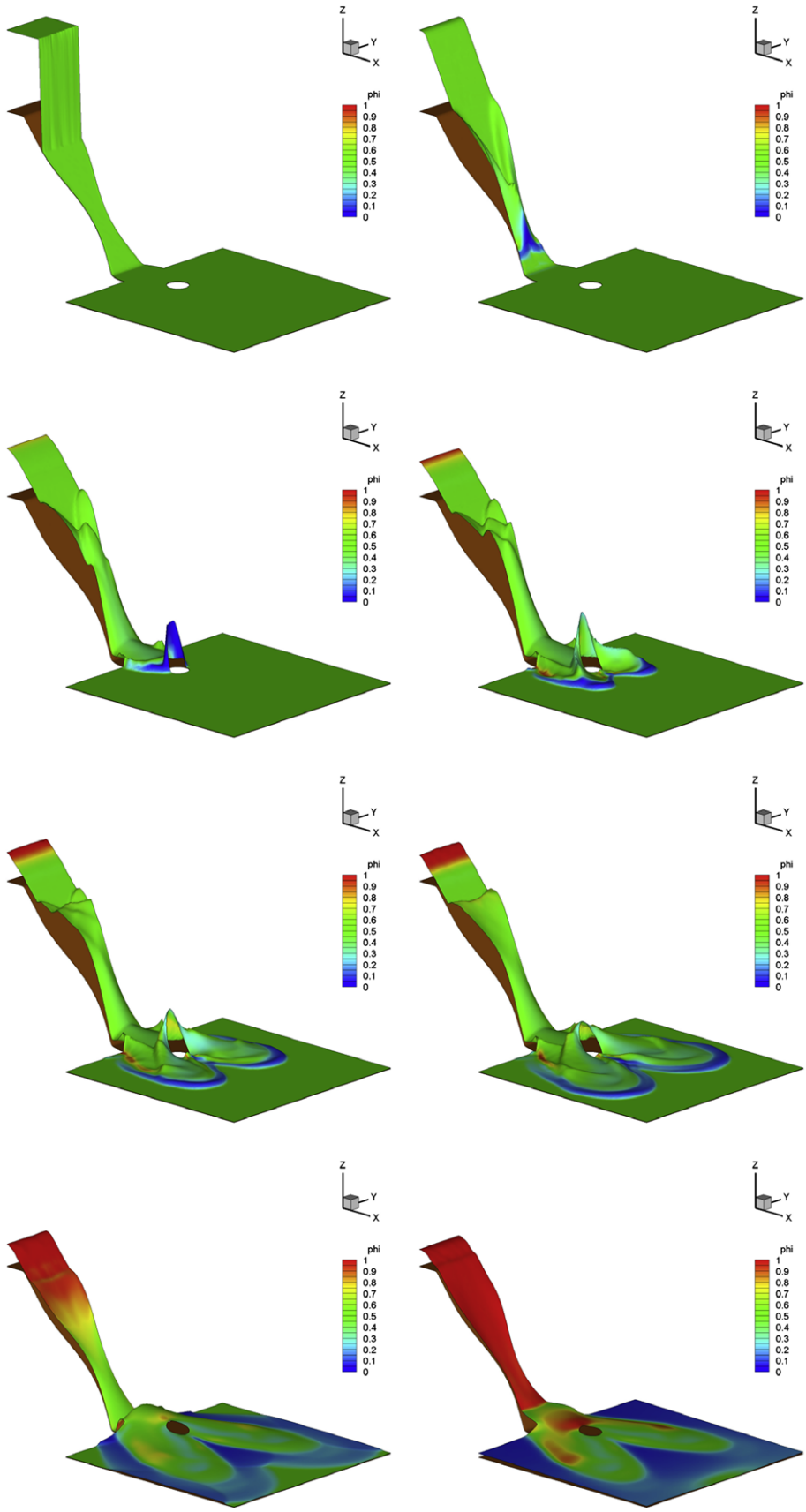

Fig. 12. 3D view of the realistic debris flow problem. The bottom topography b is shown in brown color, the colored surface represents the quantity $h + b$, and the color code indicates the solid volume fraction ϕ. The solution is depicted at times $t = 0,\ t = 1,\ t = 2,\ t = 3,\ t = 4,\ t = 5,\ t = 10$ and $t = 25$, respectively.

type method used in this article is the need of computing the eigenvalues and eigenvectors of the matrix $\widetilde{\underline{\underline{A}}}_{\Psi}(\mathscr{W}_h^-, \mathscr{W}_h^+) \cdot \vec{n}$. Since this can not be done analytically, neither for the two-layer shallow water system, nor for the two-fluid debris flow model of Pitman and Le, we use a fully numerical procedure (the **RG** subroutine of EISPACK) to compute the eigenvectors. We underline that both the two-layer shallow water system as well as the two-fluid model of Pitman and Le are not always hyperbolic, see a more detailed discussion in [28,29]. However, in all test cases shown in this paper, we never encountered any complex eigenvalues and there also was always a full set of linearly independent eigenvecturs available.

Further research will be conducted in order to construct a non-conservative equivalent of the recently developed conservative FORCE schemes on unstructured meshes [35]. In one space dimension, there have already been obtained some promising results [4,10], which extend the conservative FORCE method to non-conservative hyperbolic systems and which does *not* need the expensive numerical computation of the full eigenstructure of the non-conservative system.

Acknowledgements

The joint research presented in this paper was financed by the *Deutsche Forschungsgemeinschaft* (DFG) by the grant *DFG Forschungsstipendium* (DU 1107/1-1) as well as by the Italian ministry of research and education (MIUR) in the framework of the research project PRIN2007 and by the Spanish Government Research project MTM2006-08075.

References

[1] Balsara D. Second-order accurate schemes for magnetohydrodynamics with divergence-free reconstruction. Astrophys J Suppl Ser 2004;151:149–84.
[2] Barth TJ, Frederickson PO. Higher order solution of the Euler equations on unstructured grids using quadratic reconstruction. AIAA paper no. 90-0013, 28th Aerospace Sciences Meeting; January 1990.
[3] Bermúdez A, Vázquez ME. Upwind methods for hyperbolic conservation laws with source terms. Comput Fluids 1994;23:1049–71.
[4] Canestrelli A, Siviglia A, Dumbser M, Toro EF. A well-balanced high order centered scheme for nonconservative systems: application to shallow water flows with fix and mobile bed. Adv Water Resour 2009, in press. doi:10.1016/j.advwatres.2009.02.006.
[5] Castro MJ, Fernández E, Ferreiro A, Parés C. Two-dimensional sediment transport models in shallow water equations. a second order finite volume approach over unstructured meshes. Comput Meth Appl Mech Eng 2009, in press.
[6] Castro MJ, Fernández E, Ferriero A, García JA, Parés C. High order extensions of Roe schemes for two dimensional nonconservative hyperbolic systems. J Sci Comput 2009;39:67–114.
[7] Castro MJ, Gallardo JM, López JA, Parés C. Well-balanced high order extensions of Godunov's method for semilinear balance laws. SIAM J Numer Anal 2008;46:1012–39.
[8] Castro MJ, Gallardo JM, Parés C. High-order finite volume schemes based on reconstruction of states for solving hyperbolic systems with nonconservative products. Applications to shallow-water systems. Math Comput 2006;75:1103–34.
[9] Castro MJ, LeFloch PG, Muñoz-Ruiz ML, Parés C. Why many theories of shock waves are necessary: convergence error in formally path-consistent schemes. J Comput Phys 2008;227:8107–29.
[10] Castro MJ, Pardo A, Parés C, Toro EF. On some fast well-balanced first order solvers for nonconservative systems. Math Comput, accepted for publication.
[11] de la Puente J, Dumbser M, Käser M, Igel H. Discontinuous Galerkin methods for wave propagation in poroelastic media. Geophysics 2008;73: T77–97.
[12] Dumbser M, Balsara D, Toro EF, Munz CD. A unified framework for the construction of one-step finite-volume and discontinuous Galerkin schemes. J Comput Phys 2008;227:8209–53.
[13] Dumbser M, Enaux C, Toro EF. Finite volume schemes of very high order of accuracy for stiff hyperbolic balance laws. J Comput Phys 2008;227:3971–4001.
[14] Dumbser M, Käser M. Arbitrary high order non-oscillatory finite volume schemes on unstructured meshes for linear hyperbolic systems. J Comput Phys 2007;221:693–723.
[15] Dumbser M, Käser M, Titarev VA, Toro EF. Quadrature-free non-oscillatory finite volume schemes on unstructured meshes for nonlinear hyperbolic systems. J Comput Phys 2007;226:204–43.
[16] Dumbser M, Moschetta JM, Gressier J. A matrix stability analysis of the carbuncle phenomenon. J Comput Phys 2004;197:647–70.
[17] Dumbser M, Munz CD. Building blocks for arbitrary high order discontinuous Galerkin schemes. J Sci Comput 2006;27:215–30.
[18] Gallardo JM, Parés C, Castro MJ. On a well-balanced high-order finite volume scheme for shallow water equations with topography and dry areas. J Comput Phys 2007;227:574–601.
[19] Harten A, Engquist B, Osher S, Chakravarthy S. Uniformly high order essentially non-oscillatory schemes, III. J Comput Phys 1987;71:231–303.
[20] Hu C, Shu CW. Weighted essentially non-oscillatory schemes on triangular meshes. J Comput Phys 1999;150:97–127.
[21] LeFloch PG. Shock waves for nonlinear hyperbolic systems in nonconservative form. Institute for Math. and its Appl., Minneapolis, Preprint 593.
[22] LeVeque RJ. Balancing source terms and flux gradients in high-resolution Godunov methods: the quasi-steady wavepropagation algorithm. J Comput Phys 1998;146:346–65.
[23] Dal Maso G, LeFloch PG, Murat F. Definition and weak stability of nonconservative products. J Math Pures Appl 1995;74:483–548.
[24] Muñoz ML, Parés C. Godunov method for nonconservative hyperbolic systems. Math Model Numer Anal 2007;41:169–85.
[25] Noether E. Invariante Variations probleme. Nachrichten von der Gesellschaft der Wissenschaften zu Göttingen, mathematisch-physikalische Klasse, 1918, pp. 235–257.
[26] Parés C. Numerical methods for nonconservative hyperbolic systems: a theoretical framework. SIAM J Numer Anal 2006;44:300–21.
[27] Parés C, Castro MJ. On the well-balance property of roe's method for nonconservative hyperbolic systems. applications to shallow-water systems. Math Model Numer Anal 2004;38:821–52.
[28] Pelanti M, Bouchut F, Mangeney A. A Roe-type scheme for two-phase shallow granular flows over variable topography. Math Model Numer Anal 2008;42:851–85.
[29] Pitman EB, Le L. A two-fluid model for avalanche and debris flows. Philos Trans Roy Soc A 2005;363:1573–601.
[30] Press WH, Teukolsky SA, Vetterling WT, Flannery BP. Numerical recipes in Fortran 77, vol. 1. Cambridge (MA): Cambridge University Press; 1996.
[31] Quirk J. A contribution to the great riemann solver debate. Int J Numer Meth Fluids 1994;18:555–74.
[32] Rhebergen S, Bokhove O, vander Vegt JJW. Discontinuous Galerkin finite element methods for hyperbolic nonconservative partial differential equations. J Comput Phys 2008;227:1887–922.
[33] Stroud AH. Approximate calculation of multiple integrals. Englewood Cliffs (NJ): Prentice-Hall; 1971.
[34] Titarev VA, Toro EF. ADER schemes for three-dimensional nonlinear hyperbolic systems. J Comput Phys 2005;204:715–36.
[35] Toro EF, Hidalgo A, Dumbser M. FORCE schemes on unstructured meshes I: Conservative hyperbolic systems. J Comput Phys 2009;228:3368–89.
[36] Toumi I. A weak formulation of Roe's approximate Riemann solver. J Comput Phys 1992;102:360–73.
[37] van der Vegt JJW, vander Ven H. Space–time discontinuous Galerkin finite element method with dynamic grid motion for inviscid compressible flows I. General formulation. J Comput Phys 2002;182:546–85.
[38] van der Ven H, van der Vegt JJW. Space–time discontinuous Galerkin finite element method with dynamic grid motion for inviscid compressible flows II. Efficient flux quadrature. Comput Meth Appl Mech Eng 2002;191: 4747–80.
[39] Woodward P, Colella P. The numerical simulation of two-dimensional fluid flow with strong shocks. J Comput Phys 1984;54:115–73.